Chapter 13

The Porous Carbon Nanotube-Cellulose Papers as Current Collector and Electrode for Lithium Ion Battery and Supercapacitor Applications

Xiaogang Sun, Manyuan Cai, Long Chen,
Zhiwen Qiu, Jie Wang, Xu Li and Wei Chen

Additional information is available at the end of the chapter

http://dx.doi.org/10.5772/intechopen.71916

Abstract

Lithium ion batteries (LIB) and supercapacitors (electric double-layer capacitors (EDLCs) and lithium ion capacitors (LIC)) are the most energy storage service for mobile application. Lithium ion batteries are currently the most popular type of battery for powering portable electronic devices and are growing in popularity for defense, automotive and aerospace applications. The investigation of supercapacitors (SCs) has also achieved significant progresses. Although they have shown remarkable commercial successes, the electrodes and their constituent materials are still the subject of intensive research. Our research focused on a new type of carbon nanotube-cellulose composite materials as current collector of LIBs and as electrodes of SCs for improving and enhancing the energy/power density and cyclic performance of them. Carbon nanotubes (CNTs) have been widely used as conductive agent for both anodes and cathodes to replace super carbon black to satisfy the multifunctional requirements for LIBs.

Keywords: carbon nanotube, cellulose, lithium ion battery, collector, paper, supercapacitor

1. Applications of carbon nanotubes (CNTs) in lithium ion battery and supercapacitor

Lithium ion batteries (LIBs) and supercapacitors (SCs) are considered to be the most promising energy storage devices because of their relatively high energy density, good cycle

performance, power performance, longer service life, and green environmental characteristics. LIBs have a broad application prospects in portable electronic equipment, electric vehicles, and hybrid vehicles [1, 2].

The electrodes of LIB commonly use copper foil or aluminum foil as a current collector, and the active material is coated on the current collector. Carbon nanotubes (CNTs) have unique features of one-dimension, large surface area and high conductivity, which contribute to electrochemical performance of LIBs and SCs [3–5]. Thus, many investigations in terms of electrode materials are focused on CNTs. Compared with aluminum foil or copper foil, metal-free current collector is a research hotspot, CNT film or cellulose papers used as negative electrode, or anode current collector was applied in flexible lithium ion battery in many researches [6, 7]. CNT-cellulose papers (CNTCPs) are very good host for activated materials, which have a porous structure, easy formability, flexibility, and excellent physical and chemical properties. The porous CNTCP has excellent flexibility and conductivity. It has a broad application prospect for LIB applications including lithium-sulfur battery [1–15], Nano-SnO_2 anode [16–43], silicone anode [44–56], Li/CFx battery [57–63], and supercapacitors [64–80]. In this paper, we report the porous CNTCP applications as current collector and electrode for lithium ion battery and supercapacitor, respectively. Moreover, the CNTs used in this study are whisker multiwalled carbon nanotubes.

The fabrication process of the papers is simple and scalable, similar to those technology widely used for paper making in industry. The porous CNTCP with interconnected channel has high surface area and high electrical conductivity. It was considered as potential current collector and electrode for LIBs and SCs.

2. Fabrication and characterization of CNTs and CNTCPs

The synthesis of CNTs in the present investigation was synthesized in a vertical tubular reactor. An organic-metallic compound (ferrocene) was used as catalyst precursor, toluene as carbon feedstock, sulfur as growth promotion agent, and hydrogen as carrier gas.

The microfeed pump was used to feed the toluene solution and organic metal compound into reactor at a rate of 30 ml/min. The mass flow instrument was used to add hydrogen to the reactor at a rate of 40 ml/min. The generation temperature of CNTs is about 1200°C. The graphitization treatment of CNTs was operated in graphite resistance furnace.

CNTCPs were prepared by the following process: The CNT powders were dispersed by sonication and high speed cutting in distilled water for 2 h, respectively. The surfactant of polyvinylpyrrolidone (PVP) was added to improve the dispersion performance. Cellulose fibers were prepared through smashing napkins by high-speed shearing for 3 h. Both were fully dispersed and mixed by high-speed shear and sand milling in deionized water to form a suspension with a ratio of 1:1. The mixed slurry of CNTs and cellulose fibers was infiltrated by vacuum filtration, and the as-produced CNT paper (AMP) was obtained by peeling it off from the filter paper after drying at 60°C for 12 h. A randomly interwoven fiber mats were peeled from filter cloth and carbonized at 1460°C in vacuum condition. **Figure 1(a, b)** shows the SEM and HRTEM images of CNTs, and **Figure 1(c, d)** shows the SEM images of CNTCP and FCNT.

http://dx.doi.org/10.5772/intechopen.71916

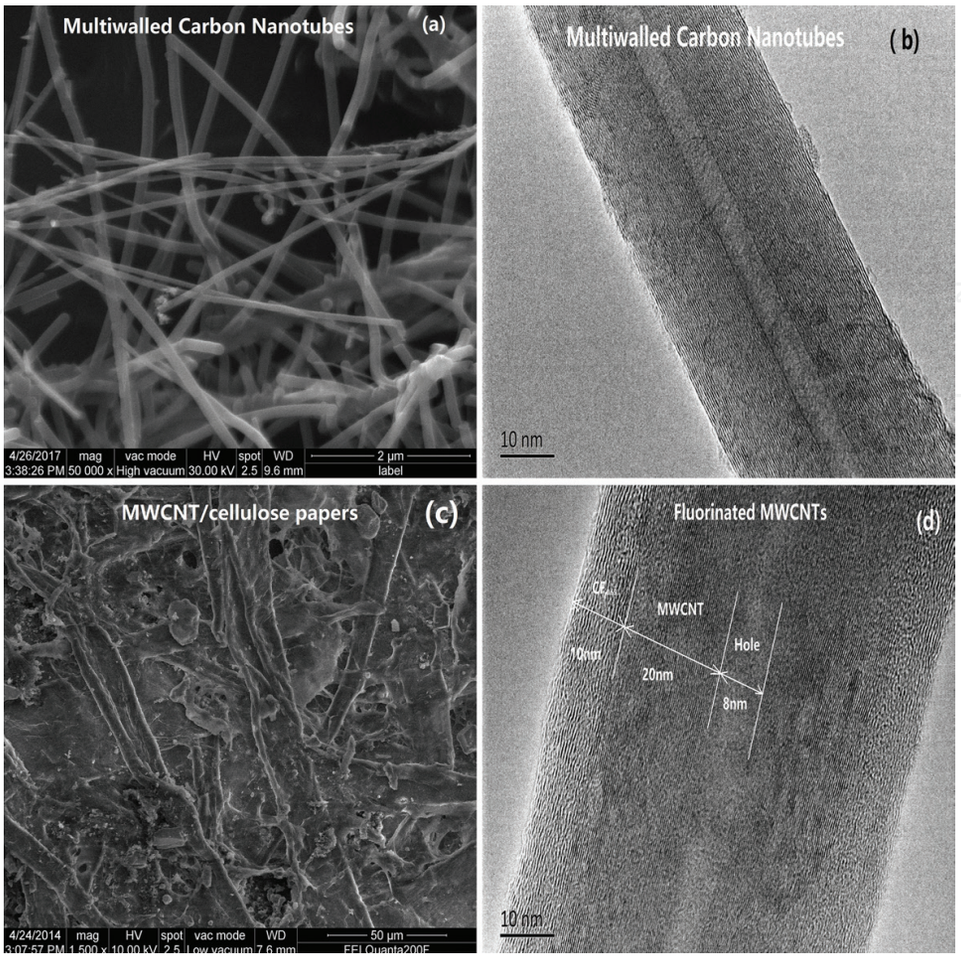

Figure 1. (a) SEM of CNTs, (b) HRTEM of CNT, (c) SEM of CNTCP, and (d) FCNT.

The CNTs were characterized by field-emission scanning electron microscopy (FE-SEM, JSM-6701F), transmission electron microscopy (TEM, JEOL JEM-2010FEF), X-ray diffraction (XRD, DI SYSTEM), Raman spectrometry (SENTERRA), and thermogravimetry (TGA, PYRIS DIAMOND). The microstructure of the electrodes was investigated by scanning electron microscopy (FE-SEM, JSM-6701F). Fourier transformation infrared spectra (FTIR, Nicolet 5700) were recorded. Electrical conductivity was measured by the conventional four-probe DC method (St2258C four-point probe meter).

3. The CNTCP used as current collector and electrode for LIBs and SCs application

3.1. CNTCP used to replace aluminum foils for Li-S cells

3.1.1. Experiment

3.1.1.1. Preparation of composite host

CNTs were synthesized by chemical vapor deposition and treated at a high temperature of 3000°C for graphitization. The CNTs powder was dispersed in deionized water with a dispersant

of sodium dodecylsulfate (SDS) ($CH_3(CH_2)_{11}OSO_3Na$). The paper cellulose is made of soaked soft wood pulp in deionized water. The CNTs dispersion liquid and the cellulose pulp were mixed by high-shear emulsifier to form suspension for 3 h. The suspension liquid of cellulose and CNTs pulp was infiltrated by vacuum filtration. A randomly interwoven fiber mat was obtained. The paper was rolled and tailored as current collector for activated materials.

3.1.1.2. Preparation of sulfur electrodes

Sulfur and conductive additive of carbon black (CB) were mixed by balling for 2 h at 230 r/min. Then, the slurry of sulfur and CB was prepared by ultrasonication and high-shear process with N-methyl-2-pyrrolidone (NMP) as solution and PVDF as binder. The ratio of S:CB:PVDF = 36:54:10. The blended slurry was coated on to aluminum foils (S-Al electrode) and porous composite host (S-CNTs/CP electrode). The electrodes were dried under vacuum at 60°C for 24 h.

3.1.1.3. Assembling of cell and electrochemical measurements

The tailored of S-Al electrode and S-CNTs/CP electrode were respectively used as working electrodes. Li metal foils were used as the counter electrodes, and Celgard 2300 was used as the separator. CR2025 coin-type cells were assembled in an Ar-filled glove box (MBRAUN LABSTAR, Germany). The electrolyte was prepared by dissolving lithium bistrifluoromethane sulfonylimide (LITFSI) and lithium nitrate ($LiNO_3$) in 1,2-dimethoxyethane (DME) and 1,3-dioxolane (DOL) (1:1 ratio, by volume). The electrochemical characterization of the cells was measured by a cell tester (CT-3008 W-5V5mA-S4). Electrochemical impedance spectroscopy (EIS) and cyclic voltammetry (CV) were performed within a potential window of 1.8–2.6 V by an electrochemical workstation (CHI 660B). The specific capacity was calculated according to the mass of the sulfur in the host. The charge and discharge current density was set at 0.05 C to 2C.

3.1.2. Results and discussion

SEM image in **Figure 2(a)** shows that the CNTs have a distinct one-dimension line structure and were not entangled. They can be more easily dispersed than common carbon nanotubes (CCNTs). TEM image of the CNTs is shown in **Figure 2(b)**. It can be observed that the CNTs have a straight and clear texture with high crystallinity.

Figure 3(a) shows SEM image of top surface of as-produced CNTs/CP host with a random-in-plane web-like network structure. The CNTs/CP host demonstrated homogenous incorporation of CNTs in the cellulose fibers network. **Figure 3(b)** shows the cross-section image of CNTs/CP host. The figures clearly displayed porous network structure which provided sufficient void space for loading a large amount of sulfur and accommodating the volume expansion of sulfur during cycles. The coarse surface and interconnected channel permit good penetration of the electrolyte and sulfur. The pore size distribution of as-produced CNTs/CP host is shown in **Figure 3(c)**. From the picture, we can see that the host has big porosity. The special surface area of the host reached 25.6 m^2/g.

http://dx.doi.org/10.5772/intechopen.71916

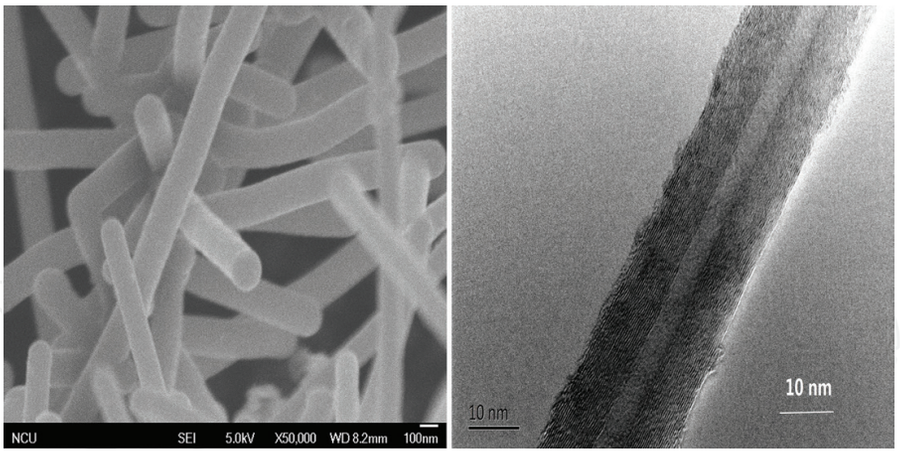

Figure 2. SEM (a) and TEM (b) images of CNTs.

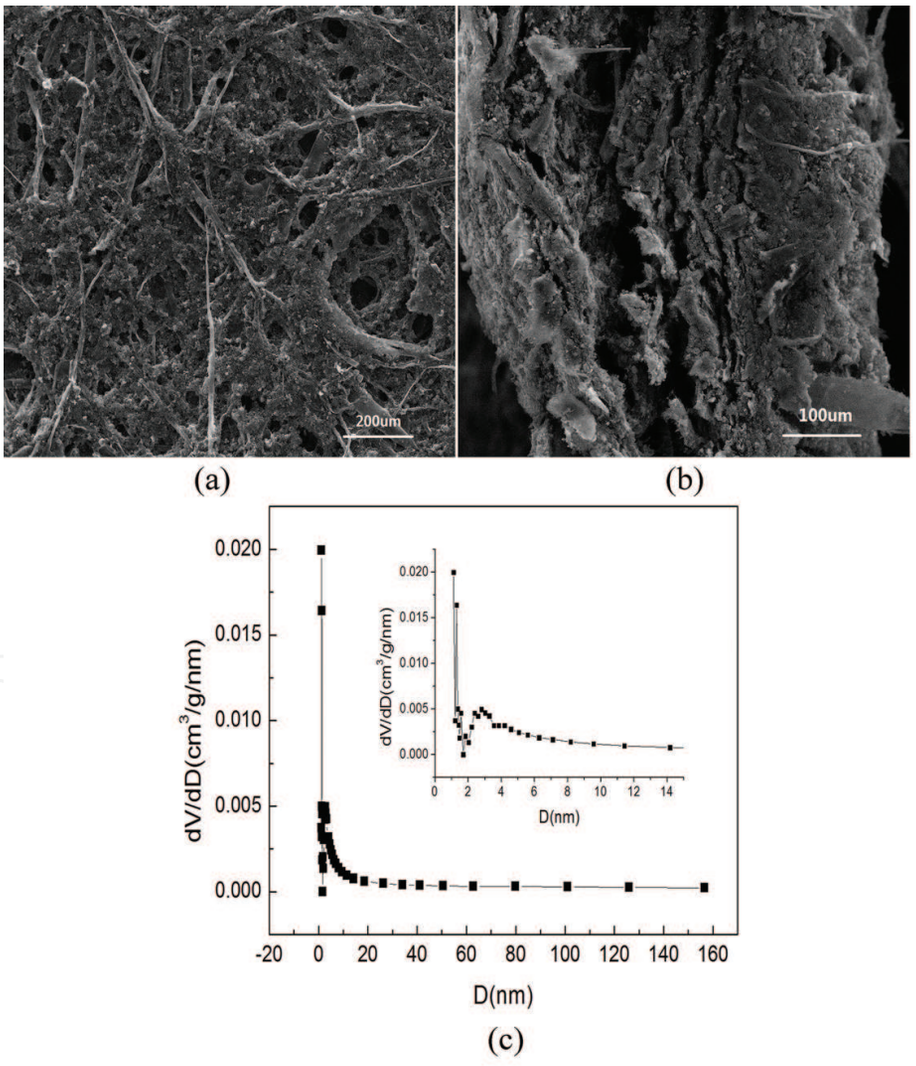

Figure 3. SEM images of CNTs/CF host (a) surface, (b) cross-section, and (c) pore size distribution.

It was known that a sufficient amount of electrolyte is especially required for a high sulfur-loaded cathode during the electrochemical transformation between sulfur and polysulfides [81, 82]. Therefore, the superior electrolyte absorbability of the S-CNTs/CP contributes to stabilized electrochemical reactions in high sulfur-loaded electrodes. S-CNTs/CP can also suppress the diffusion of polysulfides, which resulted in superior cycling stability.

Figure 4(a) shows the cross-section images of S-CNTs/CP electrode. It can be observed that sulfur embedded into micropores of host has a uniform distribution. This made an intimate contact between sulfur and host. The interfacial contact area enhanced and interface resistance decreased substantially, which are highly desirable for high rate charge-discharge cycles. The energy dispersive spectra (EDS) of cross-section of S-CNTs/CP electrode (**Figure 5**) further demonstrate that sulfur embedded into CNTs/CP host which was attributed to good cycle stability. **Figure 4(b)** shows the cross-section images of S-Al electrode. It can also be observed

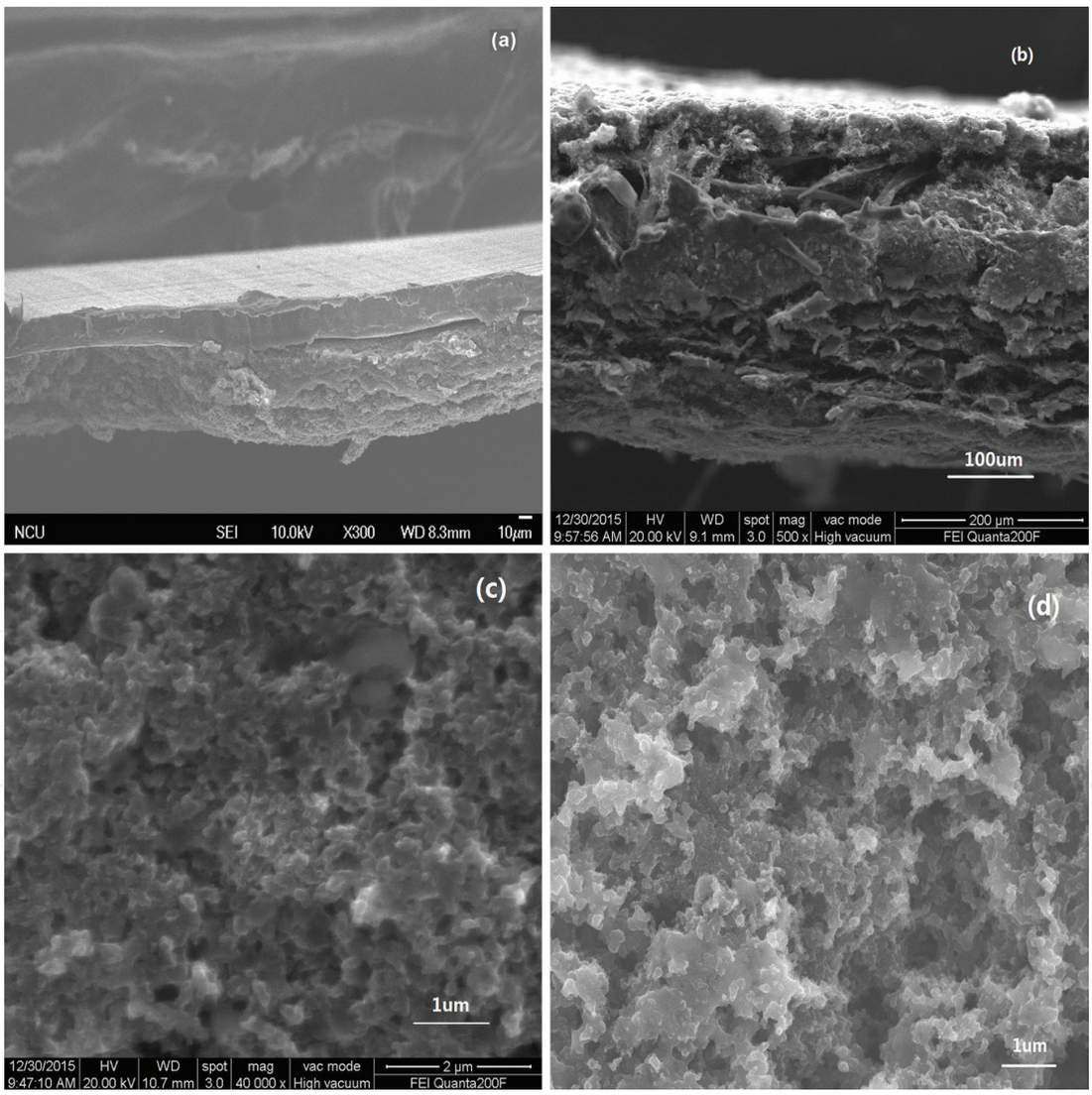

Figure 4. SEM of CNTs/CP and Al foil loaded with sulfur (a) S-Al cross section, (b) S-CNTs/CP cross section, (c) S-Al top after cycles, (d) S-CNTs/CP top after cycles.

http://dx.doi.org/10.5772/intechopen.71916

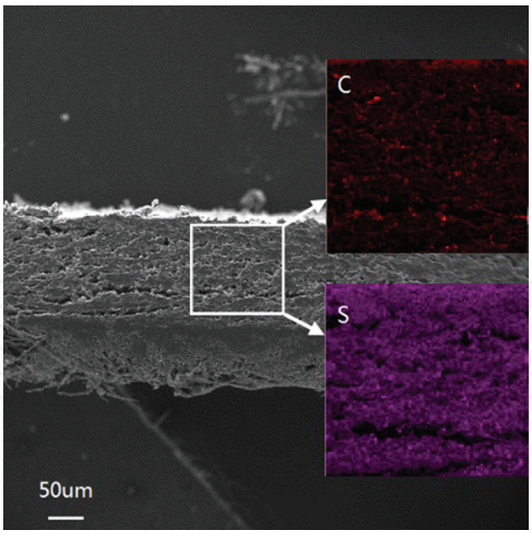

Figure 5. The EDS images of cross section of S-CNTs/CP electrode.

that there will be visible pores between the interface of sulfur and Al foil, which resulted in increasing interface resistance. **Figure 4** shows the morphologies of two electrodes of S-Al electrode (c) and S-CNTs/CP electrode (d) after 60 cycles. It was observed that S-CNTs/CP electrode maintains a smooth and unbroken surface, while the S-Al electrode shows an uneven surface. Due to weak binding force and low affinity between sulfur and Al foil, sulfur was exfoliated from Al foil during cycles. **Figure 6** shows the first three cyclic voltammetry (CV) curve of the S-CNTs/CP electrode at a scan rate of 0.05 mV /S in the voltage range of 1.8–2.6 V. In the first electrode scan, two characteristic reduction peaks at 2.29 and 1.99 V can be observed. The reduction peak at about 2.3 V belongs to the reduction of element sulfur to long-chain LiPSs (Li_2S_n, 4<n<8). The peak at 2.0 V indicated the reduction of lithium polysulfide to short-chain lithium sulfide (Li_2S_2, (Li_2S) [81–84]. The two oxidation peaks were

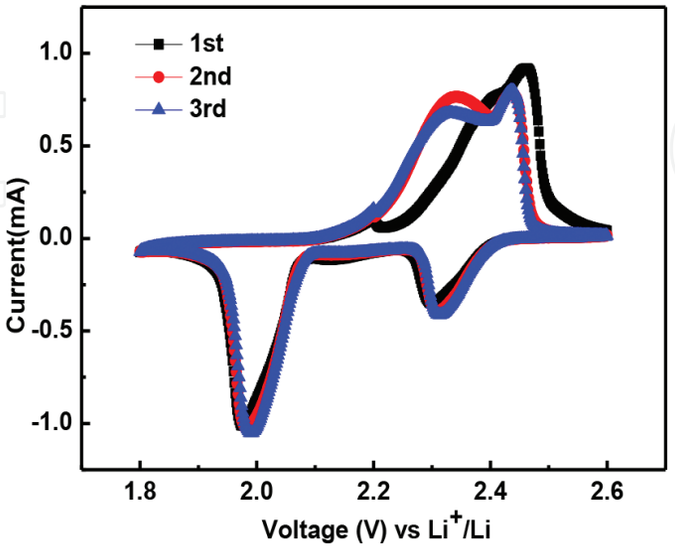

Figure 6. The first three cycles of CV curves of S-CNTs/CP electrode.

represented at 2.3 and 2.4 V. Li_2S_n (n > 2) was formed at 2.3 V, and elemental sulfur was generated at 2.4 V. The electrodes displayed the almost identical CV curves from beginning of the second cycle. The overlap of subsequent oxide and reduction peaks suggested that the electrodes have high electrochemical stability and good reversibility. It also indicated that the interconnected porous 3D structure is a quite good support of sulfur to prevent shuttle effect and maintain high utilization of sulfur.

Figure 7(a) shows the discharge-charge curves of S-Al electrode at first, second, and 10th at the current rate of 0.05 C, respectively. It can be seen that there are two plateaus for each discharge curve at 2.3 and 2.1 V, respectively. The plateaus of 2.3 V represented the formation of long-chain polysulfides (Li_2Sn, 4<n<8) with shorter flat range. The plateaus of 2.1 V represented conformation of short-chain sulfides of Li_2S_2 and Li_2S [13] with longer flat range. The first discharge specific capacity reached around 1085 mAh/g, which represented a 64.7% utilization of sulfur (1675 mAh/g). But the capacity rapidly faded to 884.5 mAh/g at second cycle. The capacity only maintained at 714 mAh/g after 10th cycle, which is only 65.8% of first discharge capacity. The utilization of sulfur was also declined to 42.6%.

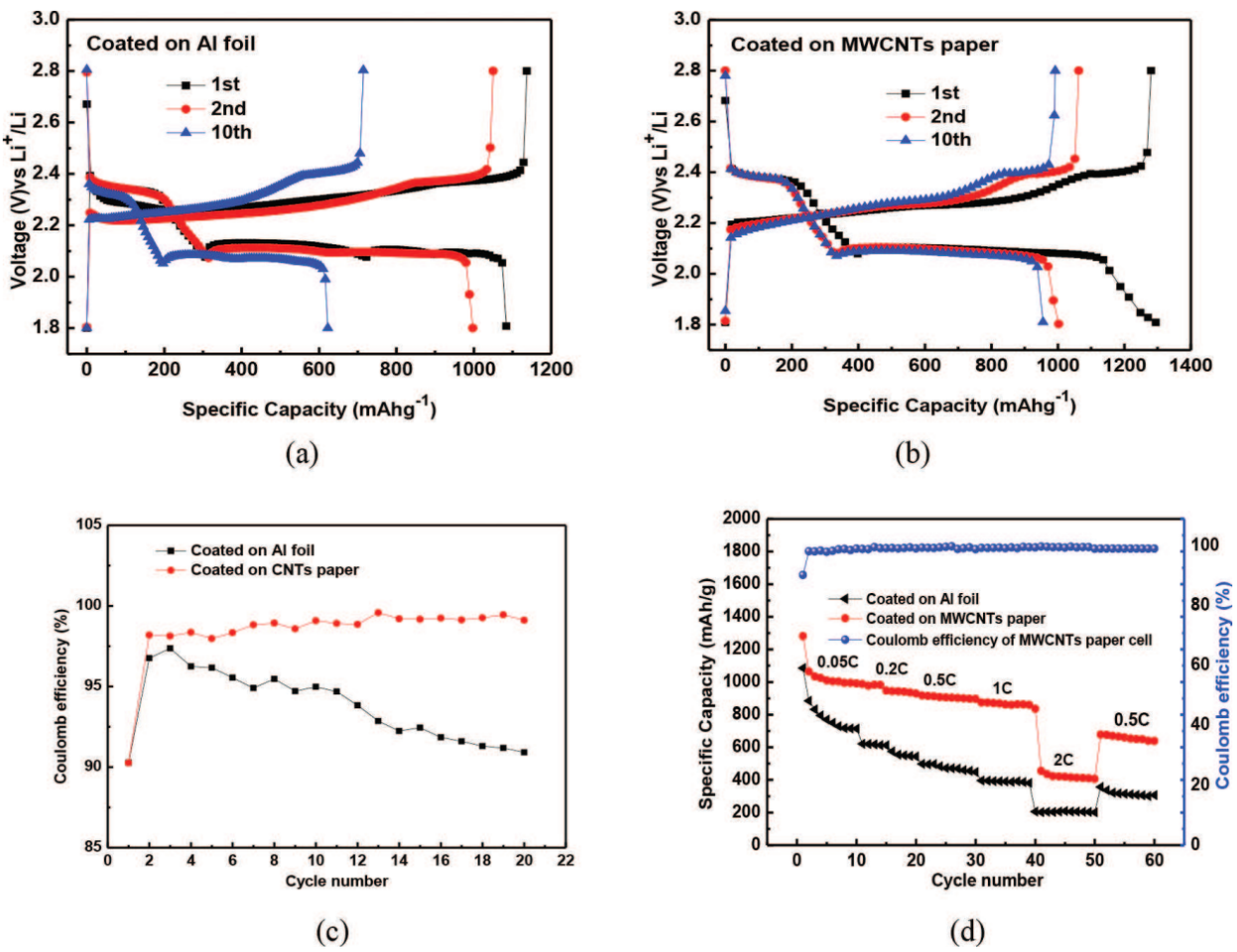

Figure 7. Charge/discharge of S-Al electrode (a) and S-CNTs/CP electrode (b), coulombic efficiency (c), cycle and rate performance of (d).

http://dx.doi.org/10.5772/intechopen.71916

Figure 7(b) shows the discharge-charge curves of S-CNTs/CP electrode. The galvanostatic discharge-charge profiles displayed a similar curve as S-Al electrode. These plateaus are also consistent well with the current peaks in the CV curves (**Figure 6**). But the discharge profiles of S-CNTs/CP electrode displayed highly overlapped voltage plateaus at 2.1 V. It was considered that the short-chain sulfides taken place in almost same potential upon cycling, which revealed little kinetic barriers for conformation of short-chain sulfides [85–87]. The first discharge specific capacity of S-CNTs/CP electrode reached around 1282 mAh/g, which represented a 76.5% utilization of sulfur (1675 mAh/g). The capacity still maintained at 991.7mAh/g after 10 cycles, which is 77.3% of first discharge capacity. The Coulombic efficiency maintained over 98% from second cycle beginning (**Figure 7c**). After 20 cycles, the Coulombic efficiency of S-Al electrode dropped sharply to 90%, while S-CNTs/cellulose electrode still held 98%. The S-CNTs/cellulose electrode achieved better electrochemical performance than S-Al electrode. The cycle and rate performance of the both electrodes were shown in **Figure 7(d)**. It was shown that the discharge capacity of S-Al electrode declined rapidly. The capacity only maintained around 180 mA/g at the rate of 2C after 50 cycles, while S-CNTs/CP electrode exhibited a stabile discharge capacity of 400mAh/g at 2C. When the charge-discharge rate returned to 0.5C, the discharge capacity recovered to 600mAh/g with a Coulombic efficiency of 97.5%, which suggested excellent redox stability of the S-CNTs/CP electrode. The excellent electrochemical performance of S-CNTs/CP electrode could be ascribed to its good conduction, abundant active interface, and porous interconnected structure. The unique structure can not only increase the absorption of electrolyte and loading of sulfur but also provide stable transfer channels for ions and electrons. The diffusion of LiPSs also was confined effectively.

Figure 8 illustrates the electrochemical impedance analyses of the S-CNTs/cellulose and S-Al electrode before cycles and after cycles, respectively. The experimental data demonstrated that the electrochemical impedance spectra of the two electrodes consist of a single-depressed

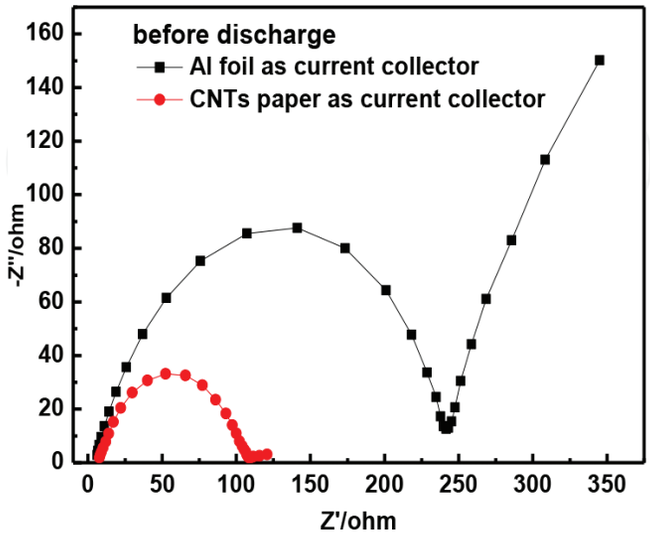

Figure 8. The electrochemical impedance spectra before (a) and after (b) cycles.

semicircle in the high-to-medium frequency region and an inclined line at low frequencies. Before cycle, the charge-transfer resistance of S-CNTs/CP electrode reached 110 Ω, which is lower than 240 Ω of S-Al electrode. After 60 cycles, the charge-transfer resistance of S-CNTs/CP electrode declined to 60 Ω, while the charge-transfer resistance of S-Al electrode only reduced to 210 Ω (**Figure 8b**). This can be attributed to the porous structure of the electrode and 3D conductive network of the electrode, which provides good electrolyte wetting and infiltrating and fast charge transport channel. The polysulfides in the S-CNTs/CP electrode suffer from less dissolution in the electrolyte due to the confinement which prevent and relieve shuttle effect. EDS (**Figure 5**) also identify that sulfur was well distributed in S-CNTs/CP electrode. The strong interaction between sulfur encapsulated in the micropores of the electrode and CNTs is beneficial to improve the electron transfer. The electrolyte and sulfur incorporated in the interconnected channel of porous electrode enhanced the mobility of lithium ions for the electrochemical reaction. The novelty host can also accommodate the volume change of sulfur and alleviate stress generated by volume expansion during cycling.

3.1.3. Conclusions

The S-CNTs/CP electrode with high porosity and interconnected channel was fabricated as host of sulfur for Li-S batteries. This unique hierarchical porous structure with 3D electric conductive network formed by CNTs can provide good path for the penetration of electrolyte and sulfur. The conduction of ions and electrons also were significantly improved. The unique architecture can trap elemental sulfur and LiPSs to suppress shuttle effect. The dissolution and diffusion of LiPSs were effectively checked during cycles. S-CNTs/CP electrode also demonstrated an excellent electrolyte uptake characteristic with four times higher than S-Al electrode. The high electrolyte absorbability of S-CNTs/CP electrode improved the utilization of sulfur. The porous structure can accommodate the volumetric expansion of sulfur during lithiation and alleviate stress generated by volume expansion [88]. This work provided a facile and environment-friendly technology for fabricating high-performance Li-S batteries and exhibited a promising future for practical applications.

3.2. CNTCP used to replace aluminum foils as collector and scaffold for nano-SnO_2 anode

3.2.1. Experiment

3.2.1.1. Preparation of electrode pieces anodes

The nanosized tin oxide (SnO_2) and carbon nanotubes (CNTs) were milling in a ball mill (250 r/min) for about 1 h. Solvent 1-methyl-2-pyrrolidone (NMP) and binder (PVDF) was wetted ball mill for 2 h to obtain a negative electrode slurry. Solid content is about 50 vol%. The ratio of SnO2: CNT: PVDF = 1.8 g: 0.6 g: 0.3 g was uniformly coated to a 3 μm copper foil and approximately 100 μm of CNT conductive paper, respectively. Then, drying at 60°C in vacuum atmosphere cut into φ14mm pole pieces. The tin oxide lithium battery pole piece was prepared.

http://dx.doi.org/10.5772/intechopen.71916

3.2.1.2. Assembling of cell

The tailored CNT papers were used as working electrodes, and Li metal plate was used as the counter electrode. CR2025 coin-type cells were assembled in an Ar-filled glove box (MBRAUNLABSTAR, Germany) by stacking a porous polypropylene separator. The liquid electrolyte was 1 M LiPF6 dissolved in a mixture of ethylene carbonate (EC) and dimethyl carbonate (DMC) (1:1 in weight).

3.2.1.3. Electrochemical measurements

The electrochemical characterization of the cells was measured by a cell tester (CT-3008 W-5V5mA-S4). Electrochemical impedance spectroscopy (EIS) and cyclic voltammetry (CV) were performed by an electrochemical workstation (CHI 660B). The specific capacity was calculated according to the total mass of the CNT and SnO_2.

3.2.2. Results and discussion

The morphology and microstructures of SnO_2/CNT/Cellulose electrodes were examined by scanning electron microscopy (SEM) and transmission electron microscopy (TEM).

Figure 9(a) shows cross-sectional area of CNT paper. It was exhibited that the CNT papers have a random-in-plane web-like network structure with interconnected channel. The Hierarchical open channel can store a large of SnO_2 to increase energy density. The porous paper has high special surface and can increase interface contact area of SnO_2 and support to reduce interface resistance. **Figure 9(b)** shows the SnO_2 has an average diameter of 60 nm and similar ball structure. **Figure 9(c,d)** exhibits the morphology of CNTs. It can be observed the CNTs have line structure and good aligned carbon atoms.

The electrochemical process can be summarized as following in charge-discharge for the SnO_2/CNT electrode:

Discharge and charge for CNTs.

$$\text{Discharge}: 6C + xLi^+ + xe^- \rightarrow Li_xC_6 \quad (1)$$

$$\text{Charge}: Li_xC_6 \rightarrow 6C + xLi^+ + xe^- \quad (2)$$

Discharge and charge for SnO_2.

$$\text{Discharge}: SnO_2 + 4Li^+ + 4e^- \rightarrow 2Li_2O + Sn \quad (3)$$

$$Sn + xLi^+ + xe^- \rightarrow Li_xSn\ (0 \leq x \leq 4.4) \quad (4)$$

$$\text{Charge}: Li_xSn \rightarrow Sn + xLi^+ + xe^-\ (0 \leq x \leq 4.4) \quad (5)$$

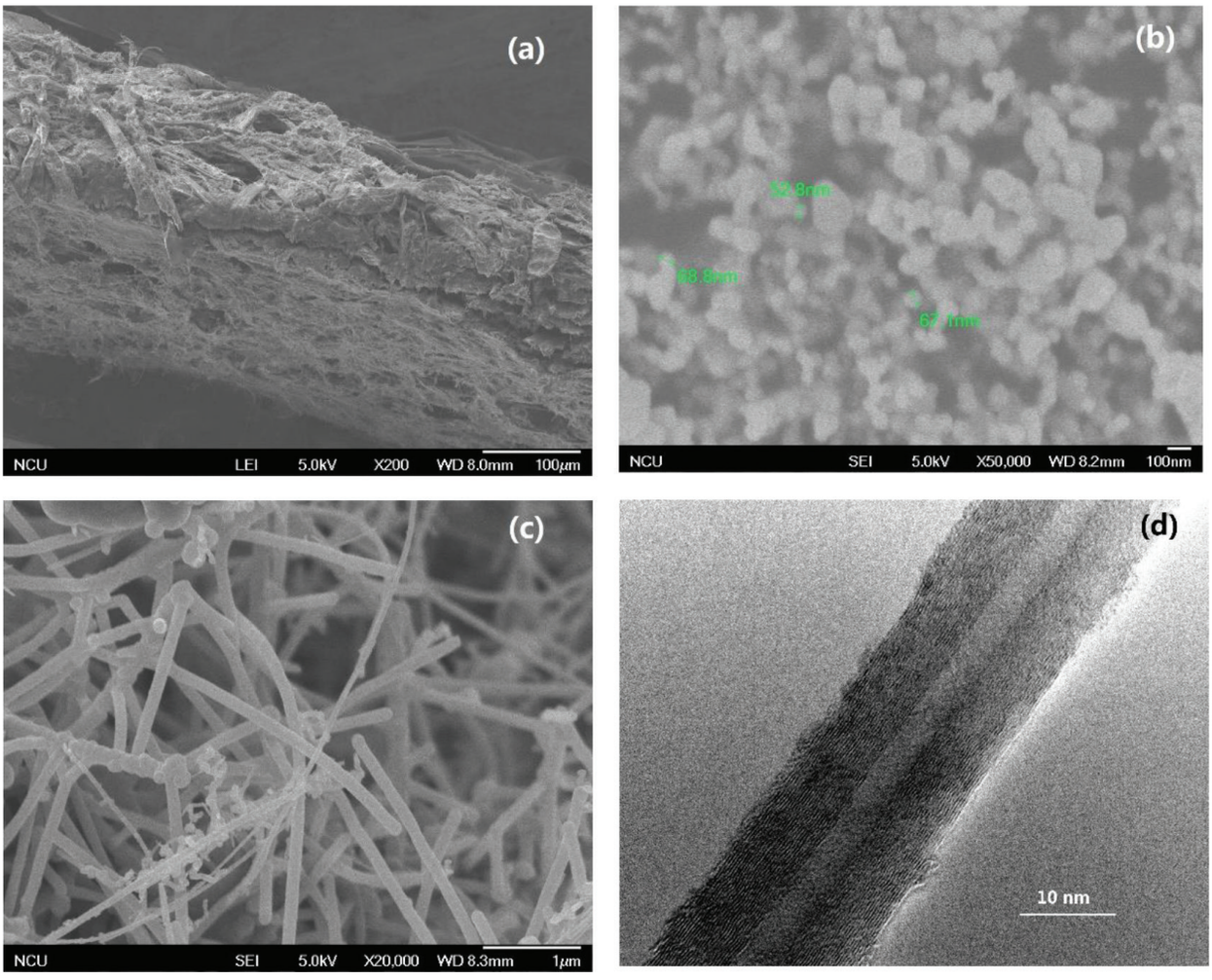

Figure 9. SEM images of porous collector (a), SnO_2 (b), CNTs (c), and HRTEM image of CNTs (d).

Cyclic voltammetry curves were recorded for SnO_2/CNT electrodes as shown in **Figure 10(a)**. The first cycle curve in the anodic sweep is substantially different from the subsequent curves. During the first oxidation scan, three characteristic oxidation peaks were observed at 0.3, 0.5, and 1.3 V. The strong peak at 0.3 V can be ascribed to lithium insertion into CNTs (Eq.(1)), which have been treated at 3000°C and obtained at very high crystallinity degree [89]. The strong peak at 0.5 V was corresponding to alloying process for forming Li_xSn alloy (Eq. (4)) [90]. The broad peak at 1.3 V can be considered to be the partly reversible reaction representing the conversion of Sn to SnO_2 (Eq. (3)) [91]. In first cathodic sweep process, sharp characteristic peaks were observed at 0.65 V. The sharp peak at 0.65 V can be ascribed to the formation of the solid electrolyte interphase (SEI) film on surface of CNTs and SnO_2 [92]. The irreversible transformation of SnO_2 to Sn was also contributed to the prominent reduction peak (Eq. (3)) [92]. The sharp reduction peak only appeared in first discharge cycle, which was originated from the initial irreversible capacity [92]. During subsequent 2nd and 3rd cycles, the CV curves were overlapped fully. This implied that the reactions in Eqs. (3) and (4) are highly reversible.

http://dx.doi.org/10.5772/intechopen.71916

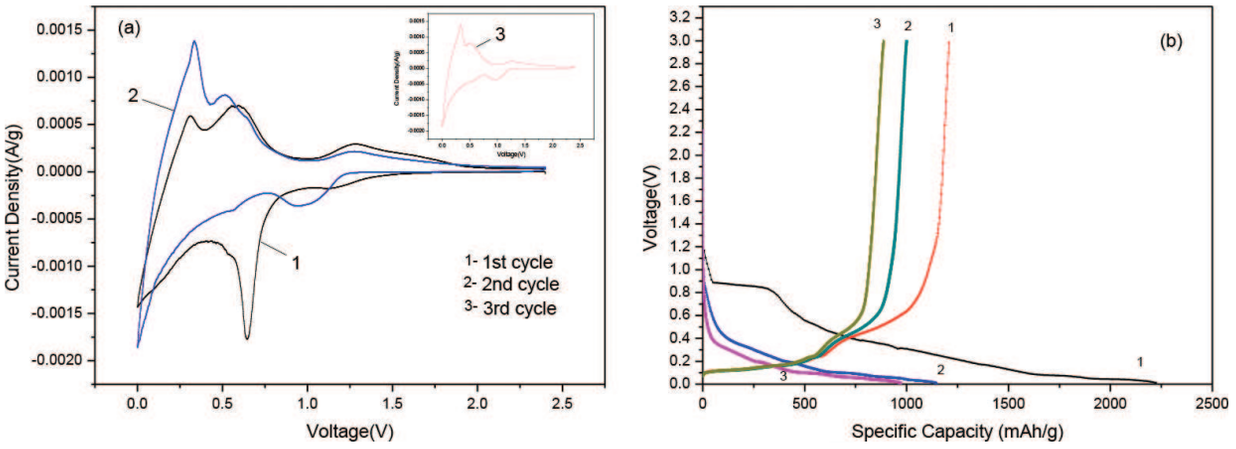

Figure 10. (a) Cyclic voltammetry curves at a scan rate of 0.1 mV/s over the potential window of 0–2.4 V. (b) the initial three galvanostatic discharge and charge profiles of the SnO_2/CNT electrode at current density of 100 mA/g.

Figure 10(b) shows the initial three galvanostatic discharge and charge profiles of the SnO_2/CNT electrode at current density of 100 mA/g. The first discharge and charge capacity reached around 2240 and 1250 mAh/g, respectively, with first coulombic efficiency of 56%. A voltage plateau at around 0.90 V can be noticed in the initial discharge process, which is attributed to the formation of Sn and Li_2O [28]. Moreover, the initial discharge capacities of 2240 mAh/g are higher than the theoretical capacity of SnO_2 (1494 mAh/g) [93], which can be attributed to CNTs that have a specific capacity of 200–3000mAh/g [94], and the oxygen containing functional groups reacted with lithium ions to exhibit certain capacity and the irreversible formation of the SEI layer [95]. A discharge capacity of 1140 and 1000 mAh/g was achieved in the 2nd and 3rd cycle. With the increase of the cycle numbers, the capacity fades very slowly.

The electrochemical performances of pure SnO_2 and CNT porous composite electrode were evaluated (**Figure 11**). The pure SnO_2 and slurry (1.8 g SnO_2: 0.6 g CNT: 0.3 g PVDF) were coated on copper foil and CNT paper collector, respectively. The charge-discharge current was hold at 100 mA/g. **Figure 11** shows the capacity of pure SnO_2 cathode exhibited abrupt capacity fading at the initial stage of cycling. After 20 cycles, the capacity almost faded away completely. The cathode-doped CNTs coated on copper foil collector maintained a capacity of 200mAh/g after 20 cycles. The cathode with CNT paper as collector exhibited excellent performance. The capacity was tend to stabilization after 6 cycles and still holds a capacity of about 600mAh/g after 20 cycles. The result suggested that the porous CNT paper collector is beneficial to enhance the kinetics of electrochemical reactions between SnO_2 and lithium ions with more interface areas.

The SnO_2/CNT paper electrode presents the excellent electrochemical performance. **Figure 12(a)** shows the rate capabilities of SnO_2/CNT paper electrode at various current densities from 100 mA/g to 500 mA/g. It exhibits a first discharge capacity of 1218 100mAh/g compared with a first discharge capacity of 1050mAh/g of copper foil collector. SnO_2/CNT/cellulose electrode showed remarkably enhanced rate capability, and much better capacity retention was attained, particularly at high current densities during charging. The capacity retention holds 680 mAh/g

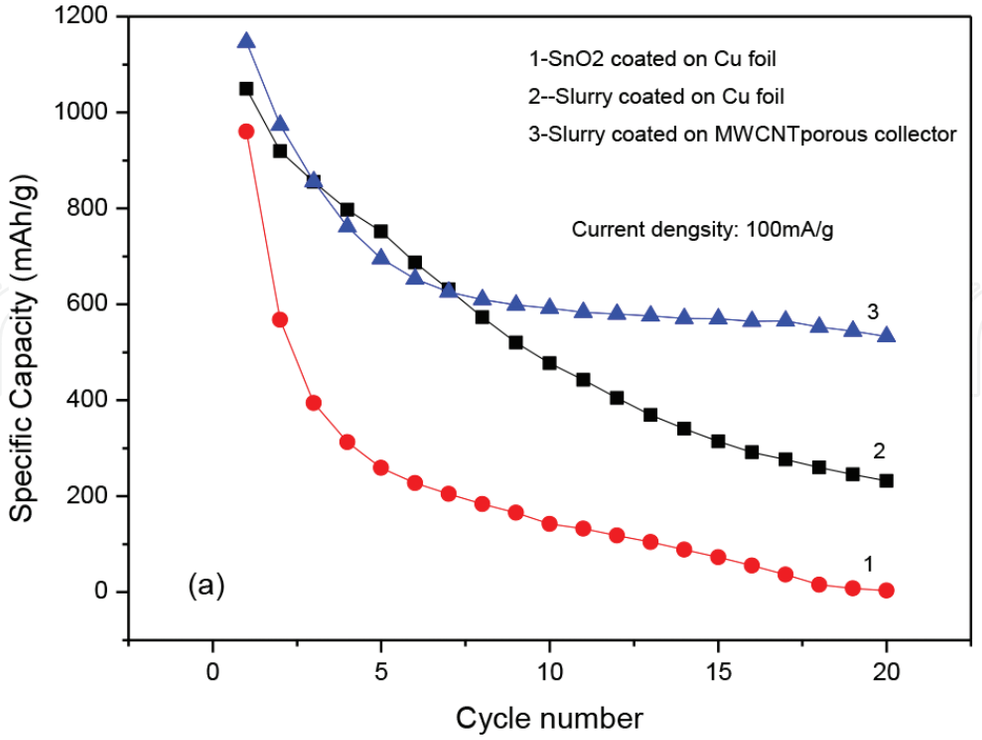

Figure 11. Cycling performance of SnO_2 coated on different collector.

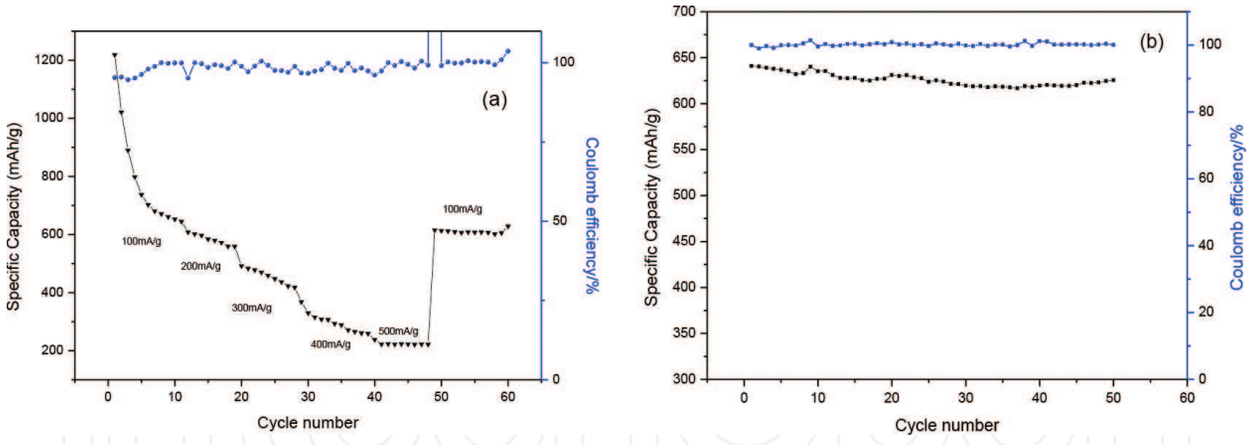

Figure 12. Cycling and rate performance of SnO_2 coated on CNT porous collector.

at 100 mA/g, 580 mAh/g at 200 mA/g, 420 mAh/g at 300 mA/g, 310 mAh/g at 400 mA/g, and 220 mAh/g at 500 mA/g. When the current density returned to 100 and 50 mA/g, respectively, the discharge capacity was recovered to 610 and 620 mAh/g in spite of subjecting to cycling at high current densities. The outstanding rate retention identified that the composite electrode is robust and highly stable even so high rate charge-discharge was tested.

The cycling performance and coulombic effect of SnO_2/CNT electrode were evaluated at 200 mA/g. As presented in **Figure 12(b)**, the capacity of electrode reduces rapidly during first

http://dx.doi.org/10.5772/intechopen.71916

6 cycles. After then, the capacity fading was quite gentle. It should be noted that the retained capacity of the electrode was approximately 500 mAh/g after 100 cycles, which is much higher than that of the commercial graphite electrode. Furthermore, the CNT electrode maintained a stable coulombic efficiency of over 98%. This suggested the SnO_2/CNT/cellulose can bear big current shock and maintain good cycle performance.

Figure 13 illustrates the electrochemical impedance analyses of the SnO_2/CNT/cellulose electrode before cycles and after cycles, respectively. The experimental data show that the electrochemical impedance spectra of the electrodes consist of a single depressed semicircle in the high-to-medium frequency region and an inclined line at low frequencies. Before cycles, the charge-transfer resistance of the electrode reached 260 Ω. But after 100 cycles, the charge-transfer resistance of the electrode drastically declined to 60 Ω. This can be attributed to the porous structure of the electrode and 3D conductive network formed in the electrode by CNTs, which provide good electrolyte wetting and infiltrating and fast charge transport channel. The porous collector provides a large of space for storage of SnO_2, and reduced element Sn can be dispersed and infiltrated into the space of the collector. This resulted in the increase of contact interface areas for activated materials and collector. The Sn (SnO_2) encapsulated in the micropores of the electrode enhanced effectively the electron transfer. This can account for the decline of charge-transfer resistance after charge/discharge cycles.

Figure 14(a) shows top surface images of SnO_2/CNT/cellulose electrodes. It can be observed that SnO_2 was embedded into micropores of CNT/cellulose electrodes. This made an intimate contact between SnO_2 and CNTs and increases interfacial contact areas. The interface electrical resistance decreased substantially, which are beneficial to high-rate charge-discharge cycles. **Figure 14(b)** shows the morphologies of SnO_2/CNT/cellulose electrodes after cycles. A smooth layer on the surface can be observed. The SnO_2 nanoparticles do not show obvious aggregation. **Figure 14(c, d)** shows the image of cross section of both electrodes. **Figure 14(c)**

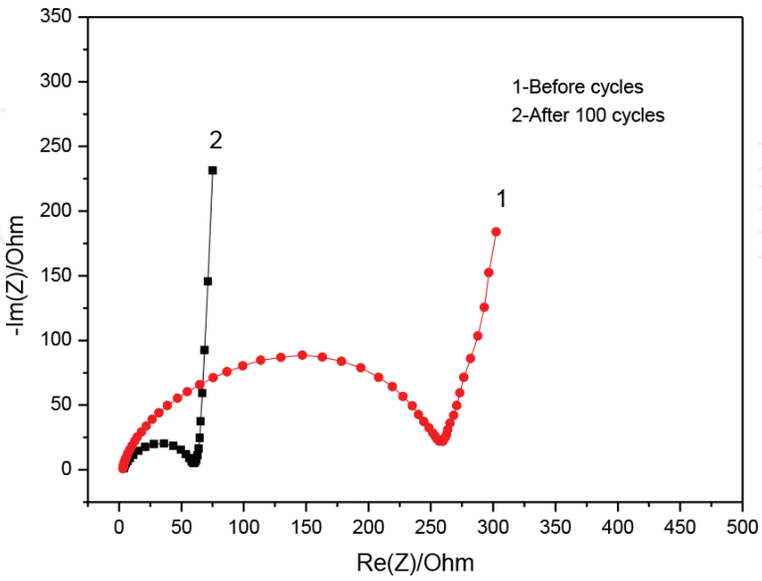

Figure 13. EIS of SnO_2 coated on CNT collector.

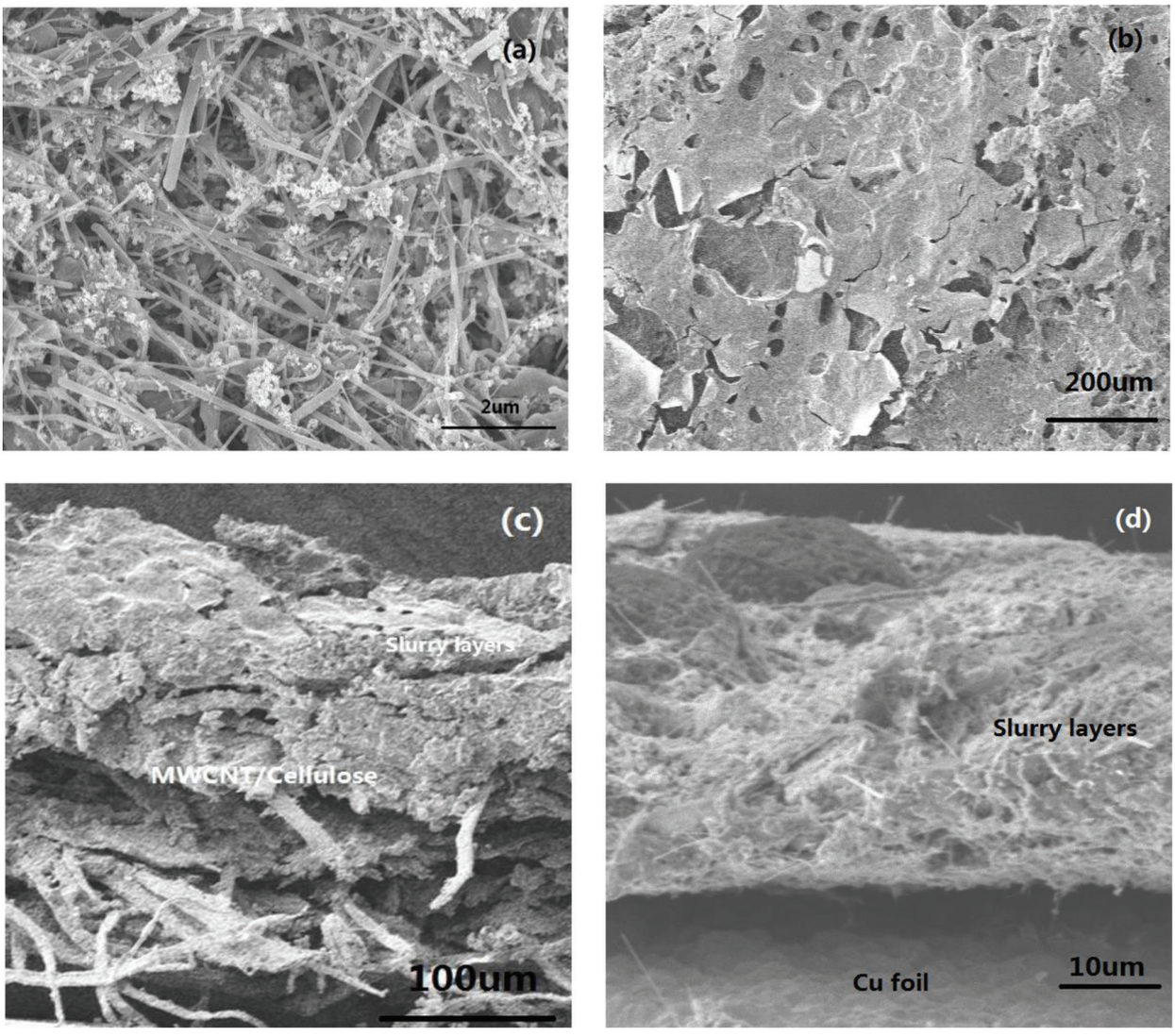

Figure 14. SEM images of SnO_2/CNT/cellulose electrodes (a) top surface before cycles, (b) top surface after cycles, (c) cross section after cycles, and (d) SnO_2/copper foil electrode cross section after cycles.

demonstrates that SnO_2 and CNT/Cellulose collector have close combination, and no cracks can be observed on interface of both after cycles. **Figure 14(c)** further revealed that SnO_2 was embedded into CNT/cellulose collector and made an intimate contact which was attributed to good cycle stability. However, SnO_2/copper foil electrode shows an obvious crack and pores on interface after cycles. It can also be observed that SnO_2 and Cu foil collector have not good affinity, and there can be visible interface pores which resulted in the decreasing contact interface. This sharply increasing of interface resistance will result in rapid fading of capacity.

Figure 15(a) shows that SnO_2 was only observed on the top of CNT porous collector. After charge-discharge cycles, SnO_2 intercalated into the interior of CNT collector and fully dispersed in the collector (**Figure 15(b)**). This can be attributed to the special interconnected channel of the CNT collector which provided and enhanced diffusion of nano-tin reduced from SnO_2 in discharging process. The homogeneous diffusion of tin increased effectively

http://dx.doi.org/10.5772/intechopen.71916

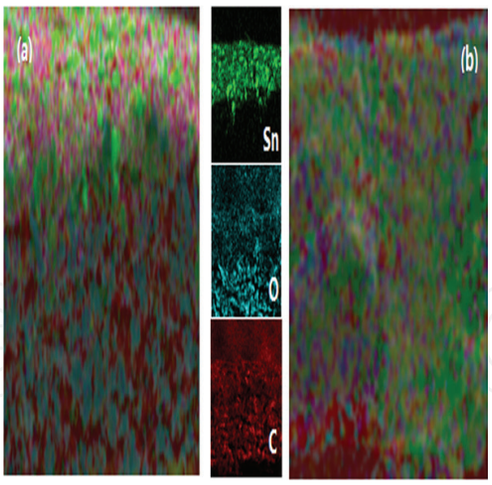

Figure 15. EDS of SnO_2/CNT porous electrodes (a) before and (b) after cycles.

contact interface areas of collector and tin dioxide and lowed interface electrical resistance. This is in full accord with EIS spectra (**Figure 13a**), which indicated that the charge transfer resistance became smaller after cycles. The diffusion also improved reversible capacity and maintained a good cycle stability from beginning of 40th cycles.

3.2.3. Conclusion

In summary, we have demonstrated a porous CNT/cellulose host to support SnO_2 as positive electrode for lithium ion battery electrode. The 3D structure with interconnected channel can load ultrahigh SnO_2 for high energy density battery. The hierarchical pores and channels can accommodate the big expansion of SnO_2 during charge/discharge and maintain a good cycle stability. SnO_2/CNT/ cellulose electrode showed remarkably enhanced rate capability and much better capacity retention. The capacity retention holds 680 mAh/g at 100 mA/g and 220 mAh/g at 500 mA/g. When the current density returned to 100 mA/g, the discharge capacity was recovered to 610 mAh/g. This suggested that the SnO_2/CNT/cellulose can bear big current shock and maintain good cycle performance. The CNT electrode also shows a stable coulombic efficiency of over 98%.

3.3. CNTCP used to replace aluminum foils as collector and scaffold for nanosilicon anode

3.3.1. Experiment

3.3.1.1. Raw materials

Commercial nanosilicon powders (purity: 99.0%, average diameter: 100 nm) and cellulose fibers were purchased in market. CNTs were synthesized by floating reactant method in a vertical tubular reactor. Benzene was used as carbon feedstock, organic-metallic compound (ferrocene) as a catalyst precursor, thiophene as growth promotion agent, and hydrogen as

carrier gas. The reaction temperature is around 1200°C. The following thermal treatment of CNTs was carried out at 3000°C for 20 h using a graphite-resistance furnace operating in a vacuum atmosphere.

3.3.1.2. Preparation of ternary electrodes

The CNTs powder was dispersed in deionized water with a surfactant of polyvinylpyrrolidone (PVP). The paper cellulose is made of napkins in deionized water. The CNTs dispersion liquid and the cellulose pulp were mixed by acute stirring. The mixed slurry of nanosilicon, CNTs, and cellulose fibers was infiltrated by vacuum. A porous mats of CNTs and cellulose fibers embedded with nanosilicon were obtained for anode applications.

3.3.1.3. Characterizations and testing

The CNTs were characterized by scanning electron microscopy (SEM), transmission electron microscopy (TEM), X-ray diffraction (XRD), Raman spectrometry, and thermogravimetry (TGA). Nanosilicon and the microstructure of the electrodes were observed by SEM.

The CR2025 coin-type cells were assembled in an Ar-filled glove box with a metallic lithium foil as the counter electrode. The electrochemical performance was measured by a cell tester with 1 M $LiPF_6$ in a mixture of ethylene carbonate (EC) and diethyl carbonate (DEC) as electrolyte. The galvanostatic charge-discharge was tested within a cut-off voltage window from 0 to 3.0 V at a current density of 80 mA/g.

3.3.2. Results and discussion

Figure 16a, b shows the morphology and structure of nanosilicon and composite anode of Si/CNT. The SEM image exhibits that the nanosilicon powders behave a polyhedral structure and an average diameter distribution of about 100 nm.

Figure 16b shows that nanosilicon is uniformly embedded in the network of CNTs. **Figure 17a** shows the morphology and structure of CNTCP with rough and porous surface. CNTs is uniformly dispersed and attached on paper fiber (**Figure 17b**). A good three-dimensional conductive network was constructed with cellulose fiber as the framework. **Figure 18** shows the galvanostatic charge-discharge curves of the Si/CNT composite anode at a current density of 80 mA/g with current collector of copper foil (CF) and CNTCP, respectively. It can be seen that CF electrode exhibited an initial discharge and charge specific capacity of 1020 mAh/g and 817 mAh/g, respectively (**Figure 18a**). The capacity rapidly faded with cycling. The capacity dropped to less than 200 mAh/g after 30 cycles. It was very evident that CF electrode exhibited very high irreversible capacity loss in cycles. The irreversible capacity is mainly from the growth of solid-electrolyte interface (SEI) films on surface of nanosilicon. The lithiation of silicon, which resulted in accumulation of Li + in silicon matrix to form Li_xSi alloy, also contributes to the big irreversible capacity. Further, owing to big volume change over 400% and press [96–98] during lithium ion insertion and extraction, the nanosilicon crystals were cracked and pulverized by press. Those produce new interface for forming SEI film. The pulverization of nanosilicon will also result in incomplete dealloying [99, 100]. The phase change of crystalline nanosilicon into amorphous state also caused

http://dx.doi.org/10.5772/intechopen.71916

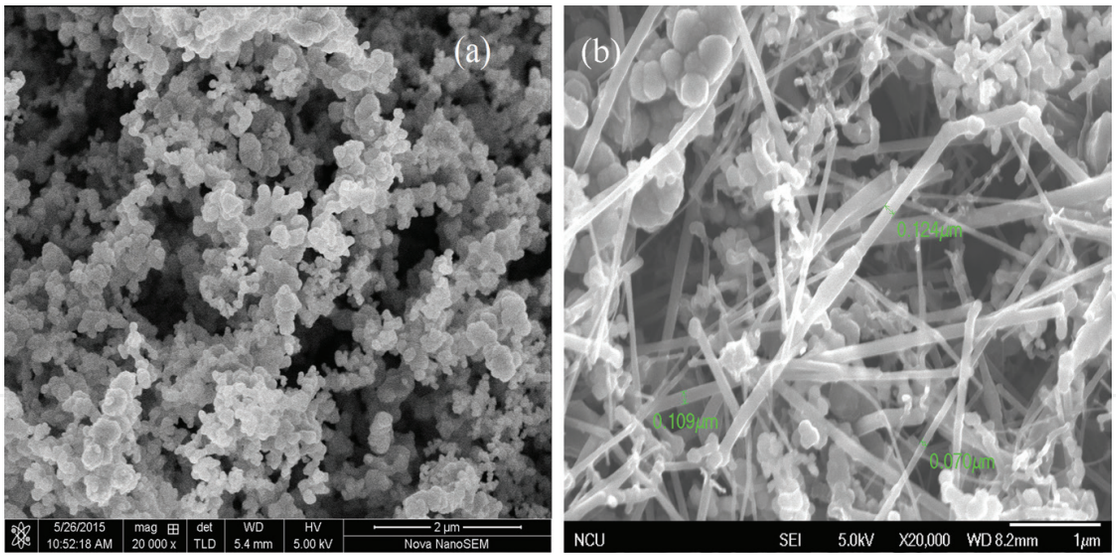

Figure 16. SEM images of nanosilicon (a) and composite Si/CNT anode (b).

some irreversible capacity loss. All those resulted in continuous capacity loss in cycles [101–103]. **Figure 18a** also exhibits an obvious charge voltage plateau at 0.5 V in first 10 cycles, which was connected to the characteristic of dealloying of Li/Si alloy. **Figure 18b** shows the discharge and charge profile of CNTCP electrode. The first discharge capacity and Coulomb efficiency of CNTCP electrode reached 2107mAh/g and 85%, respectively, which are 106 and 6% higher than those of CF electrode. CNTCP electrode becomes stable after 3 cycles, and Coulomb efficiency is closed to 100%. After 30 cycles, the specific capacity still maintained 1000mAh/g compared with only 180mAh/g of CP electrode. The cycling performances of both electrodes are showed in **Figure 18**. CNTCP electrode exhibited a 1000, 900, 500, and 200 mAh/g at a current density of 80, 200, 1000, and 2000 mA/g, respectively. When the current density reduced to 200 mA/g, the specific capacity restored 850 mAh/g after 160 cycles, which illustrated the highly reversible electrochemical behavior of CNTCP electrode. As a contrast, the capacity of CF electrode rapidly faded during cycles. The capacity declined to around 200 mAh/g at a current density of 80 mA/g after 30 cycles. The capacity

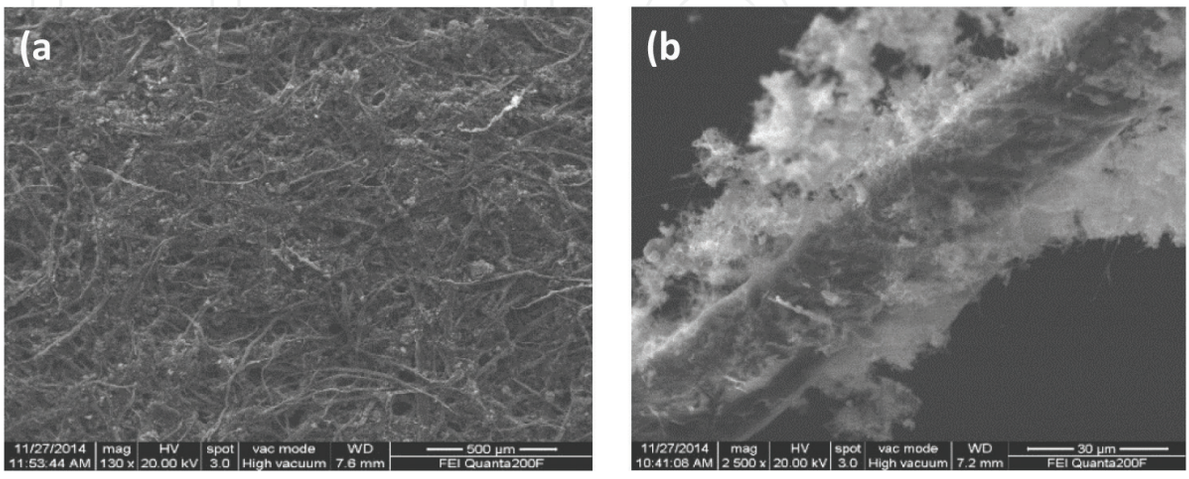

Figure 17. SEM images of CNT paper (a) top and (b) single cellulose fiber coated by MWCNTs.

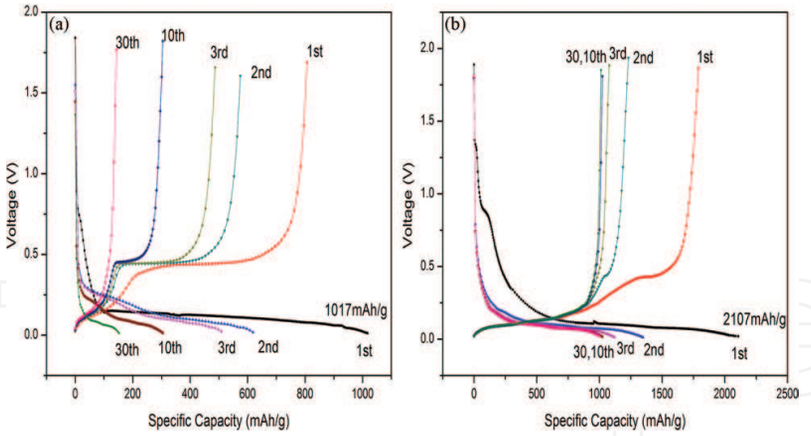

Figure 18. Discharge and charge curves of (a) copper foil cell and (b) CNT paper cell.

lowered to around 100 mAh/g after 69 cycles at a current density of 200 mA/g (**Figure 19**). The rapid decay of capacity of CF electrode was ascribed to the cracking and pulverization of silicone, which resulted in more SEI forming on interface and inefficacy of silicone, owing to big volume change and high press cannot be buffered on copper foil current collector. **Figure 20a** and **b** shows the cross-section images of CF electrode and CNTCP electrode. It can be observed in **Figure 20a** that Cu foil collector has no good affinity and nanosilicon easily produces pores on interface and big interface resistance. The sharply increasing of interface resistance will result in rapid fading of capacity. The CNTCP collector has high-porous structure and interconnected channel. Carbon and cellulose fiber have intrinsic affinity with activated materials. Nano-Si was embedded into surface

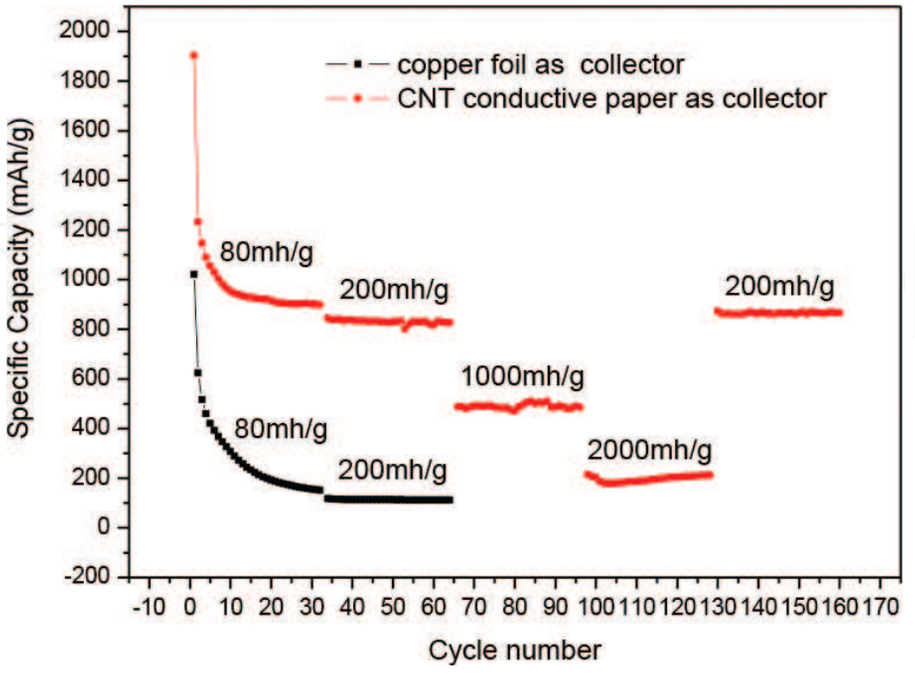

Figure 19. Cycle performance in different rate of copper foil cell and CNT paper cell.

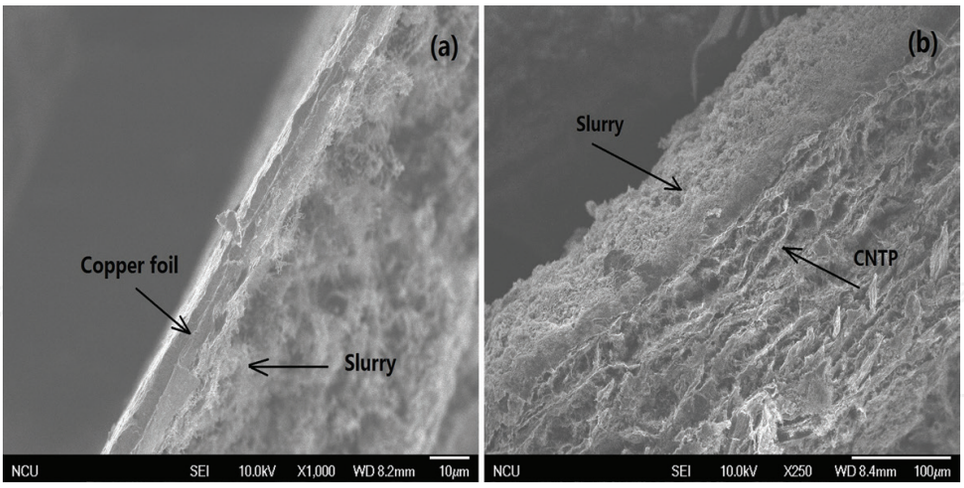

Figure 20. SEM image of interface of copper foil electrode (a), CNT paper electrode (b).

pores of CNTCP, which contributes to the low interface resistance and fast transfer of electrons and ions. The rate performance and utilization ratio of the active material were further improved.

To better understand the volume change and the stability of SEI layer, the impedance analysis was performed. All the EIS curves (**Figure 21**) show a depressed semicircle in the high frequency region and an oblique line in the low frequency domain. The CF electrode and CNTCP electrode exhibited a charge -transfer resistance 820 Ω (**Figure 21a**) and 580 Ω (**Figure 21c**) respectively. CNTCP electrode decreased by 29% than CF electrode because nano-Si was embedded into CNTCP host and effectively reduced the resistance of the coated activated material. After 30 cycles, the CNTCP electrode demonstrated significantly superiority than CF electrode. Owing to excellent accommodation of volume expansion and electrolyte absorptivity of CNTCP electrode, the charge-transfer resistance of CNTCP electrode decreased to around 30 Ω (**Figure 21c**). On the contrary, the charge-transfer resistance of CF electrode rapidly increased to around 2000 Ω (**Figure 21d**). This may be ascribed to the exfoliation of activated materials from copper collector owing to big volume expansion of silicone in cycles.

Here, CNTCP not only was used as current collector but also provides the battery with a certain capacity. **Figure 22b** revealed that CNTCP contributes 200mAh/g reversible capacity, while CF only provides a capacity of 45mAh/g [100, 104–117]. The CNTCP also consumes an irreversible capacity of 170 mAh/g (**Figure 22a**).

3.3.3. Conclusions

In the summary, the porous CNTCP was used as host of nano-Si for high-performance Li-ion battery. The CNTCP exhibited high conduction and excellent absorptivity of electrolyte. Nano-Si penetrated into the network of CNTCP to achieve a low interface resistance for high rate performance. The porous CNTCP with interconnected channel can absorb an amount of electrolyte and was wetted fully by electrolyte. All those contribute to the electrochemical performance of CNTCP electrode. The CNTCP electrode obtained a reversible capacity, as high as 1000mAh/g after 50 charge-discharge cycles. The good cycle performance is ascribed to

the accommodation and buffering effect to huge volume expansion of silicone during cycles. Therefore, the author believes that CNTCP has a good application prospect as current collector for silicon-based lithium ion batteries.

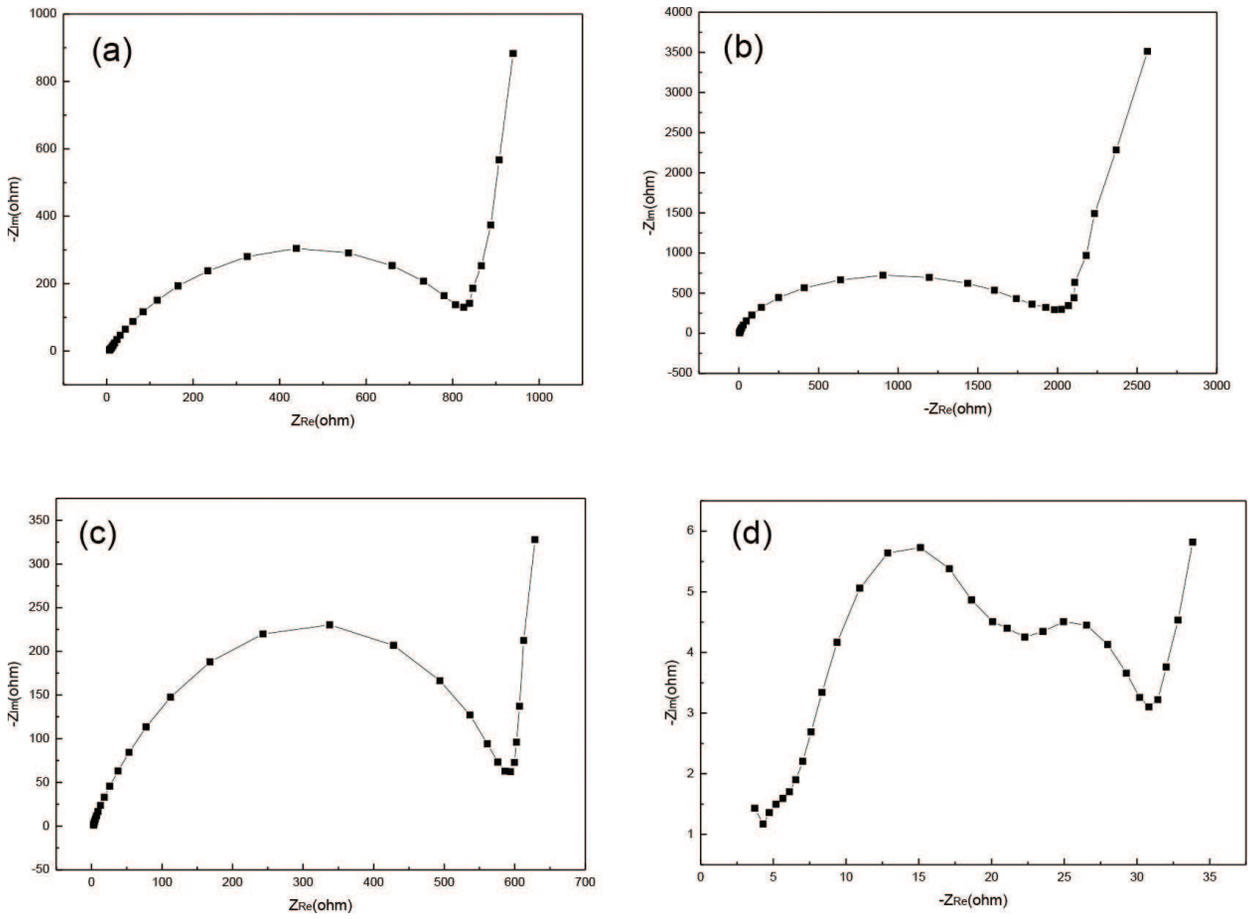

Figure 21. Impedance spectra of CF and CNT electrodes (a) fresh CF electrode (b) CF electrode after 30 cycles (c) fresh CNT electrodes (d) CNT electrodes after 30 cycles.

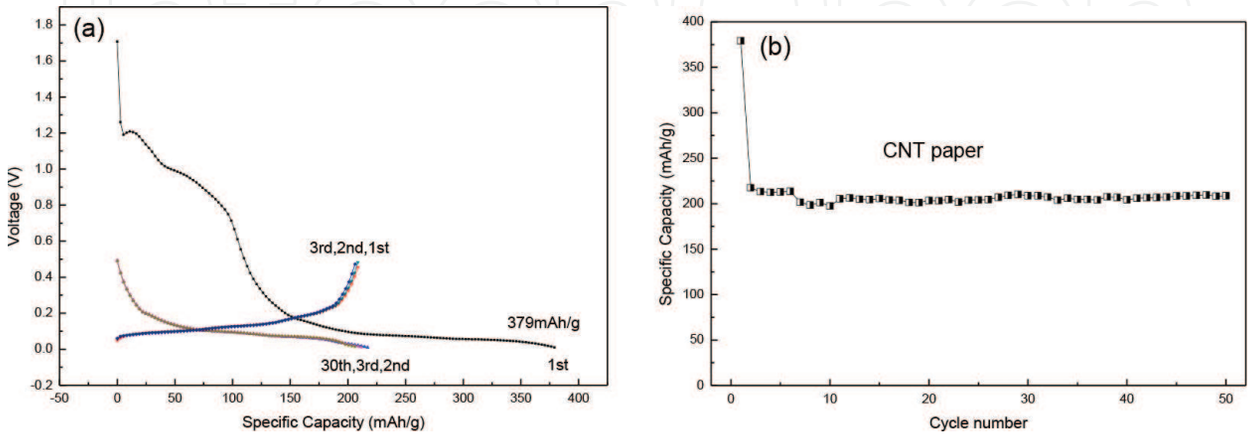

Figure 22. (a) First 30 discharge and charge curves and (b) cycle performance of CNTCP.

3.4. Primary battery based on fluorinated CNTs as cathode with CNTCP collector

3.4.1. Experimental

3.4.1.1. Fluorination of multiwalled carbon nanotubes

Three samples of fluorinated CNTs (FCNTs) were synthesized by direct fluorination of multiwalled carbon nanotubes [118]. The fluorination temperature was set at around 400°C. F/C ratio was adjusted to 0.28, 0.59, and 0.81. The FCNTs maintained a core-shell-hole structure after fluorination. The core still maintained pristine MWCNT structure with high electric conductivity and outer layers formed the structure of fluorinated carbon.

3.4.1.2. Physical characterization

Scanning electron microscopy (SEM) and high-resolution transmission electron microscopy (HRTEM) were performed to observe the core-shell-hole structure of FCNTs and analyzed their composition (EDX). F/C ratio was obtained by chemical titration method and EDX spectrometry. The change of atomic and electronic structures of FCNTs was investigated using X-ray photoelectron spectroscopy (XPS). The thermal stability of the FCNTs was investigated by thermogravimetric analysis (TGA). The weight loss of the material under argon atmosphere was recorded, while it was heated at a rate of 10°C/min from ambient temperature to 900°C. X-ray diffraction (XRD) and Raman were performed to identify the structure of FCNTs and primary CNTs.

3.4.1.3. Primary Li/CFx assemble and electrochemical characterization

The primary Li/CFx (x = 0.81) batteries were assembled with FCNTs as cathode against Li foil as anode. The electrochemical performance of the batteries was measured by cell tester (CT-3008 W-5V5mA-S4). Electrochemical impedance spectroscopy (EIS) measurements were performed on a CHI660B electrochemical workstation.

3.4.2. Results and discussion

SEM and HRTEM images of the FCNTs ($CF_{0.81}$) are presented in **Figure 23a** and **b**, respectively. After fluorination, the FCNTs exhibited a classic core-shell-hole structure. **Figure 24** shows the microstructure of FCNTs ($CF_{0.81}$). It can be clearly observed that the outer layers of CNTs were inserted by fluorine to form fluorinated carbides and inner layers hold pristine highly crystallized structure of CNTs. The exterior shell thickness of carbon fluorides ($CF_{0.81}$) was around 12 nm and internal layers of CNTs retained pristine graphitized structure with a thickness around 10 nm. The novel structure suggested that FCNTs still hold good interior electron conduction channel, even though exterior CNTs transformed into electrical insulator of carbon fluorides ($CF_{0.81}$). The central hole of CNT still remained with a diameter of 6 nm. The core-shell-hole structure means that the FCNTs maintained better electric conductivity than those of FG which is electric insulator. The central holes were contributed to the absorption of electrolyte and the diffusion of lithium ions. The novel structure can improve the conduction of both electrons but ions.

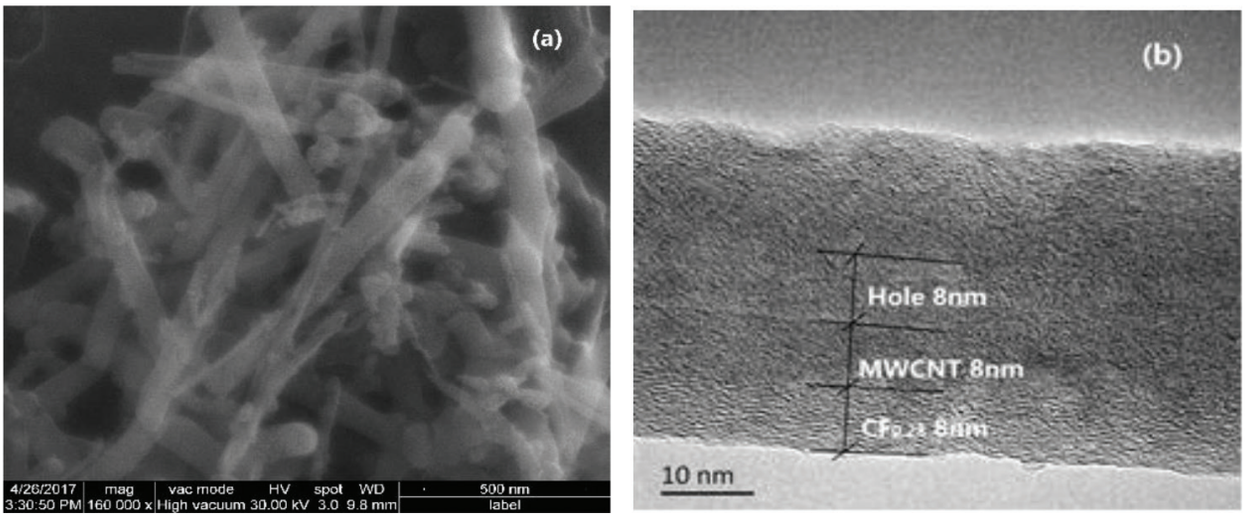

Figure 23. SEM and HRTEM of FCNTs ($CF_{0.28}$).

Carbon fluorides (CF*x*) are a type of nonstoichiometric compounds, whose thermal stability depends on the content of fluorine, the nature of carbon precursor, and the method of synthesis [8, 9]. The TGA of pristine CNTs and three FCNTs ($CF_{0.28}$,$CF_{0.56}$, and $CF_{0.81}$) are shown in **Figure 24**. It was founded that there is little loss for MWCNTs before 700°C. The weight loss of CNTs slowly began at 700°C and only has a weight loss of 10.6% at 900°C. It suggested a high heat stability of CNTs which have been treated at a temperature of 3000 and obtained very high crystallinity over 90%. The three FCNTs maintained stable before 460°C. But they began to decompose slowly when the temperature continues to increase. The decomposing of FCNTs accelerated at 500°C and terminated basically at 620°C. The primary volatile products of the thermal decomposition of the FCNTs contained CF_4 and C_2F_4, which are formed through a fluorocarbon radical process [119, 120]. It can be concluded that the $CF_{0.28}$, $CF_{0.56}$, and $CF_{0.81}$ contained around 40, 55, and 70 wt% fluorinated carbons. The following loss of

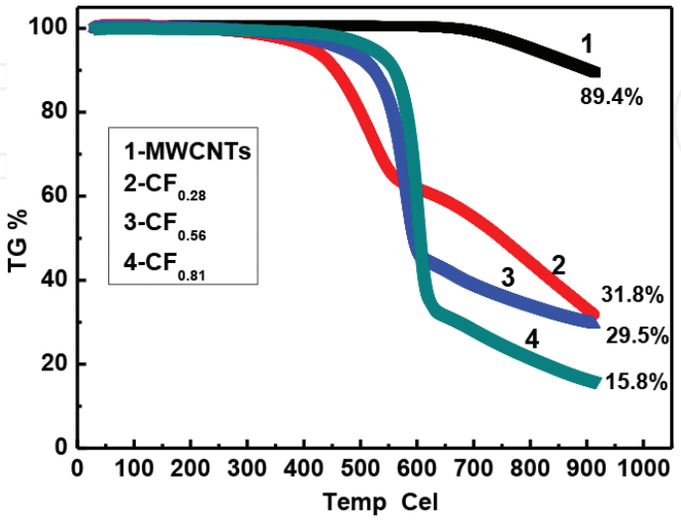

Figure 24. TGA curves of CNTs and FCNTs ($CF_{0.28}$, $CF_{0.56}$, $CF_{0.81}$) in nitrogen atmosphere from room temperature to 900°C.

weight can be ascribed to the forming of gaseous carbon-nitrogen compounds ($(CN)_x$, etc.) at temperature from 620–900°C [1]. The last remaining weight of four samples hold 89.4, 31.8, 29.5, and 15.8%, respectively, at 900°C. XRD patterns are shown for CNTs and FCNTs ($CF_{0.28}$, $CF_{0.56}$, $CF_{0.81}$) in **Figure 25a** and **b**, respectively. The stronger graphite peak (002) is observed at around 26.5° for CNTs (**Figure 25a**). But the graphite peak of FCNTs gradually weaken and finally disappeared with the enhancing fluorination of CNTs (**Figure 25a**). The outer layer structure of CNTs was destroyed with the formation of FCNTs. Fluorination only affects the outer layers of the CNTs which was resulted in destruction of graphite structure. The FCNT inner layers maintained graphite structure (**Figure 23b**). **Figure 25b** shows the Raman spectra of CNTs and FCNTs respectively. The characteristic D, G, and 2D bands are seen in two samples. Each spectrum consists of a distinctive pair of broadband at 1580 cm^{-1} (G band) and 1360 cm^{-1} (D band). The Raman peaks correspond to sp2 and sp3 carbon stretching modes, respectively. The intensity ratio of the G-band to the D-band (I_G/I_D) can be used to evaluate the graphitized degree of the samples [121, 122]. The I_G/I_D ratio of the CNTs reaches 4.3, which means a very high crystallinity. The ratio of I_G/I_D was seen to decrease to 0.66 for the FMWCNTs, as fluorine atoms are incorporated into the sp2 carbon lattice of outer layers to form amorphous sp3 structure in fluorination progresses. These results are in good agreement with XRD (**Figure 25a**).

The X-ray photoelectron spectroscopy (XPS) of the CNTs were obtained with a MultiLab 3000 spectrometer. The spectra were analyzed in order to investigate the nature of FCNTs. XPS of pure CNTs and FCNT samples are plotted in **Figure 26a**. The distinct carbon peaks of spectra were around 285.0 eV. The fluorine peaks in FCNTs were also found around 687.7 eV. With the fluorination enhanced, the F1 s peak was increased, while the intensity of the C1s peak was decreased. The detailed features for C1s peak are shown in **Figure 26b**. The peak at a binding energy (284.6 eV) in C1s spectra was assigned to sp2 hybridized carbon in CNTs. To format C-F bonds as a result of fluorination, the peak at a binding energy (289.4 eV) was assigned to sp3 hybridized carbon [118]. The peak (sp2) becomes broader and finally faded away, while the peak (sp3) was strengthened as the fluorination progresses [123]. Based on EDAX data, the four samples have been identified as $CF_{0.28}$, $CF_{0.56}$, $CF_{0.81,}$ and pure CNTs.

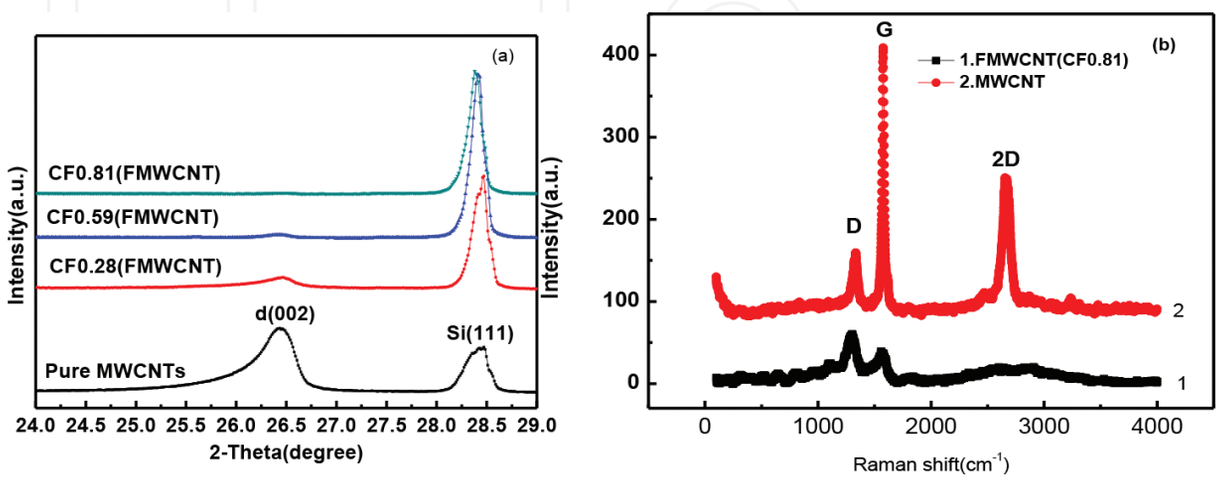

Figure 25. (a) XRD of CF0.28, CF0.59, CF0.81 and CNT and (b) Raman of CF0.81 and CNT.

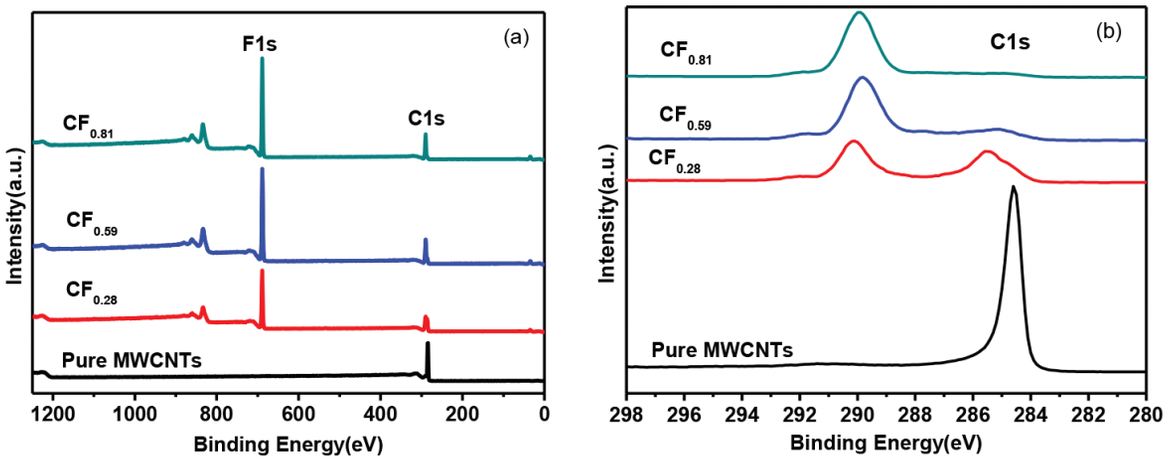

Figure 26. (a) XPS showing both F1 s and C1s peaks for pristine and FCNTs (b) detailed features for C1s peak.

The discharge profile of FG (Li/CF_1, theoretic capacity: 864mAh/g) cells is shown in **Figure 27a**. The discharge capacity reached 840 mAh/g (0.05 C), 744 mAh/g (0.1 C), 663 mAh/g (0.5 C), and 520 mAh/g (1 C). The graphite monofluoride exhibited the characteristic voltage plateau around 2.5 V at 0.05 C rate. The discharge plateau slowly dropped to about 2.0 V at discharge rate of 1 C. **Figure 27b** shows the discharge curves of FCNTs ($Li/CF_{0.81}$). The discharge starts at a higher voltage of about 3.2 V and then drops to about 2.7 V at discharge rate of 0.05 C. The discharge plateau maintained at 2.7 V with a specific capacity of 782mAh/g, which reached 98.7% of theoretic capacity of FCNT (792mAh/g for $CF_{0.81}$). The discharge plateau dropped to 2.45 V, when the discharge rate increased to 1 C from 0.05 C with a capacity of 620 mAh/g. The discharge efficiency lowered to 78.28% of theoretic capacity for carbon fluorides ($CF_{0.81}$) (**Figure 27**).

Electrochemical impedance spectroscopy (EIS) measurements were conducted in the frequency range of 100 kHz to 0.01 Hz at an excitation amplitude of 5 mV (**Figure 28**). The

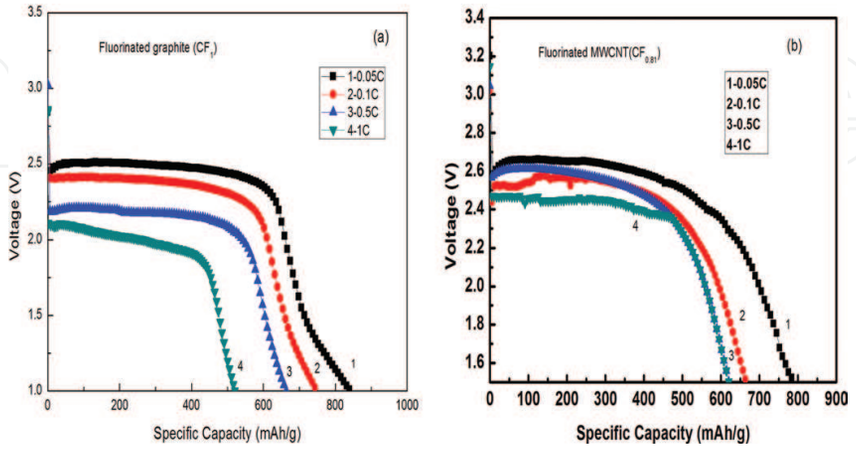

Figure 27. Discharge profile of FG and three FCNT electrodes at different rates.

http://dx.doi.org/10.5772/intechopen.71916

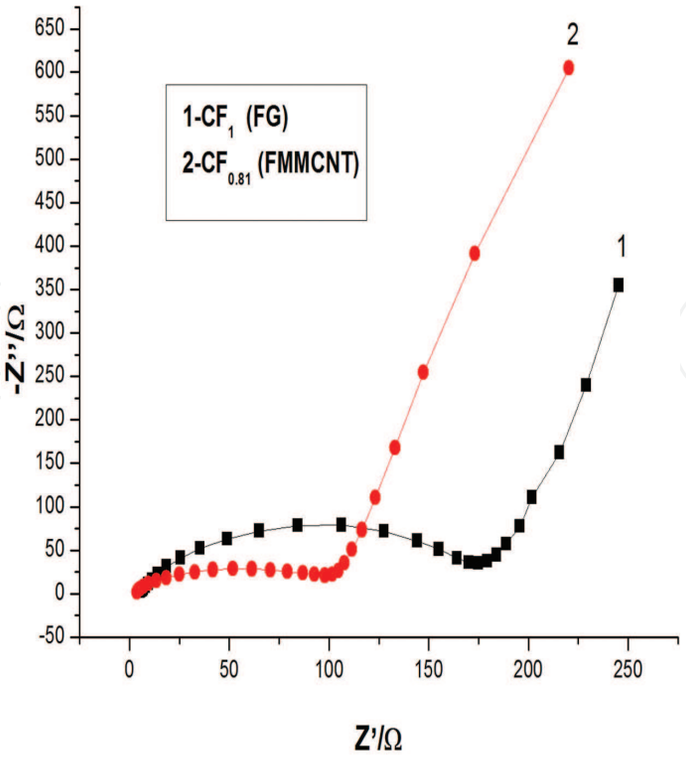

Figure 28. Electrochemical impedance spectroscopy (EIS) of $CF_{0.28}$, $CF_{0.56}$, $CF_{0.81}$ and CF_1.

Nyquist plots are composed of a semi-circle at high frequency and a linear line at low frequency. The intersection with the x-axis was corresponded to the charge-transfer resistance of the electrode with 100 and 180 Ω for $CF_{0.81}$ electrode and CF_1 electrode, respectively. It was noteworthy that the charge-transfer resistance of the electrodes increased with the increasing content of fluorine. The higher ratio of fluorine/carbon provided more activated points for the reduction of carbon fluorides to lithium fluorides and resulted in higher discharge capacity [124–128].

3.4.3. Conclusions

FCNTs exhibits a classic core-shell-hole structure. The outer layers of CNTs were Fluorinated and inner layers still maintained pristine graphitized structure integrity. The FCNTs hold good interior electron conduction channel, even though exterior CNTs transformed into electrical insulator. The core-shell-hole structure means that the FCNT maintained better electric conductivity than those of FG. FCNT exhibited better electrochemical performance than those of FG. The discharge plateau of FCNT maintained at 2.7 V (0.05C) with a specific capacity of 782 mAh/g, which reached 98.7% of theoretic capacity of FCNT (792mAh/g for $CF_{0.81}$). The discharge plateau still maintained 2.45 V at 1 C with a capacity of 620 mAh/g, and the discharge efficiency reached 78.28% compared with FG of 2 V, 520 mAh/g, and 60%, respectively. FCNTs were considered as a promise cathode materials for high performance of lithium fluoride battery.

3.5. CNTCP used as electrodes for supercapacitors

3.5.1. Experiment

3.5.1.1. Synthesis of multiwalled carbon nanotubes (CNTs)

CNTs were synthesized by floating reactant method in a vertical tubular reactor (**Figure 29**). Benzene was used as carbon feedstock, organic-metallic compound (ferrocene) as a catalyst precursor, thiophene as growth promotion agent, and hydrogen as carrier gas. The reaction temperature is around 1200°C. The following thermal treatment of CNTs was carried out at 3000°C for 10 h using a graphite resistance furnace operating in a vacuum atmosphere.

3.5.1.2. Preparation of electrodes

The CNTs powder was dispersed in deionized water with a surfactant of polyvinylpyrrolidone (PVP). The paper cellulose is made of napkins in deionized water. The CNTs dispersion liquid and the cellulose pulp were mixed by acute stirring. A vacuum filtration was used to infiltrate the mixed slurry of CNTs and cellulose fiber. Then, the formed CNTCP was carbonized at 1460°C in vacuum condition.

3.5.1.3. Material characterizations

The electrochemical characterization of the supercapacitors was measured by a cell tester (CT-3008 W-5V5mA-S4). Electrochemical impedance spectroscopy (EIS) was tested by electrochemical workstation (PARSTAT4000). Cyclic voltammetry (CV) was performed by an electrochemical workstation (CHI 660B).

3.5.1.4. Assembling of supercapacitors and testing

The tailored CNT-cellulose papers were used as the electrodes for symmetric electrochemical supercapacitors. CR2025 coin-type cells were assembled in an Ar-filled glove box (MBRAUNLABSTAR, Germany) by stacking a porous polypropylene separator. The liquid

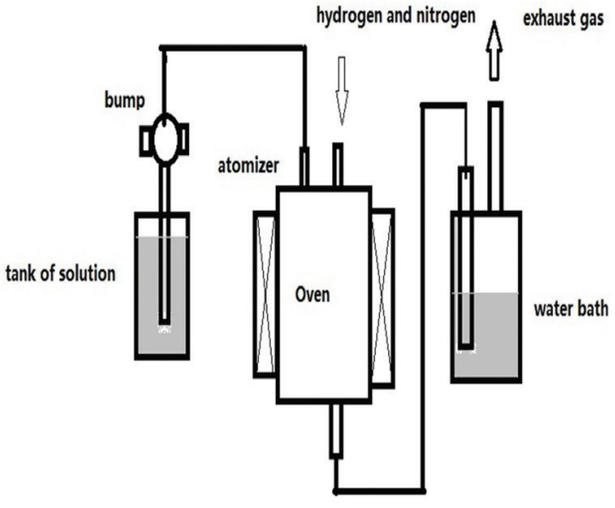

Figure 29. Schematic diagram of the setup for synthesis of CNTs.

electrolyte was 1 M LiPF6 dissolved in a mixture of ethylene carbonate (EC) and dimethyl carbonate (DMC) (1:1 in weight).

3.5.2. Results and discussion

The SEM (**Figure 30a**) images show that the CNTs have a distinct one-dimension line structure and were not entangled. They can be more easily dispersed than common carbon nanotubes (CCNTs). TEM image of the CNTs is shown in **Figure 30(b)**. It can be observed that the MWCNTs have a straight and clear texture with high crystallinity. The Raman spectra is demonstrated in **Figure 31a**. The intensity ratio of G and D band presents the degree of graphitization [121]. The I_G/I_D ratio of graphitized-CNTs was 1.81, which means a higher degree of graphitization than the raw CNTs with a 0.67 ratio of I_G/I_D. The XRD pattern (**Figure 31b**) shows the degree of graphitization as 97.25%.

The CNTCP papers are shown in **Figure 32(a, b)** and presented an obvious structure of fibers network with a 50 wt% CNT addition. **Figure 32(c, d)** shows the SEM images of carbonized CNTCP papers (CNT/CCP). It can be seen that carbonized paper fibers were coated with multiwalled carbon nanotubes. CNTs were uniformly dispersed on the surface of paper fibers.

There are five strong bands in the Raman spectra (**Figure 33**) of CNT/CP; the bands of 1100 and 2900 cm^{-1} represented the cellulose characteristic band and the bands of 1350, 1580, and 2700 cm^{-1} corresponded to the D band, G band, and 2D band of CNTs, respectively. The G band presents the ordered carbon, and D band presents the disordered carbon. The ratio of I_G/I_D was 1.18, which means CNTs have a high degree of graphitization. The CNT/CCP only has three bands of D, G, and 2D, which can be related to the reason of carbonization. The ratio of I_G/I_D was decreased to 1.02 due to higher amorphous carbon content [121, 129, 130].

Both of the CNT/CP and CNT/CCP electrodes exhibited a good layered porous structure (**Figure 34**). Most of the pore size is distributed in 2–4 nm, and CNT/CP has a much smaller pore size than CNT/CCP. Nanopores can improve the specific surface area of two papers but also conducive to the absorption of electrolytes to form electric double layer. More importantly, nanopores have played a role in helping the diffusion of electrolyte. Resulting in charged ions can pass through the 3D porous electrode, which can greatly reduce the charge transfer resistance.

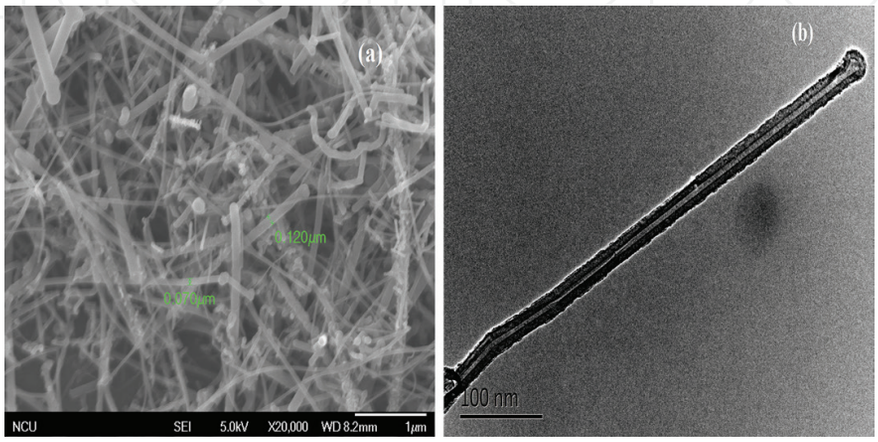

Figure 30. SEM and TEM images of CNTs.

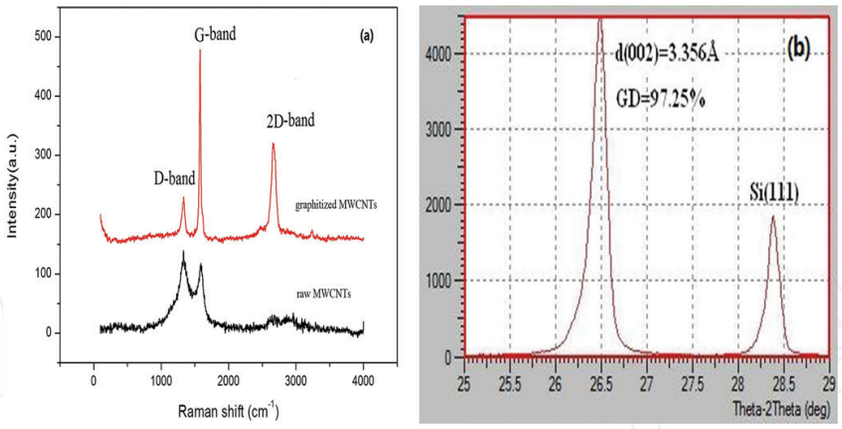

Figure 31. XRD pattern and Raman spectrometry of CNTs.

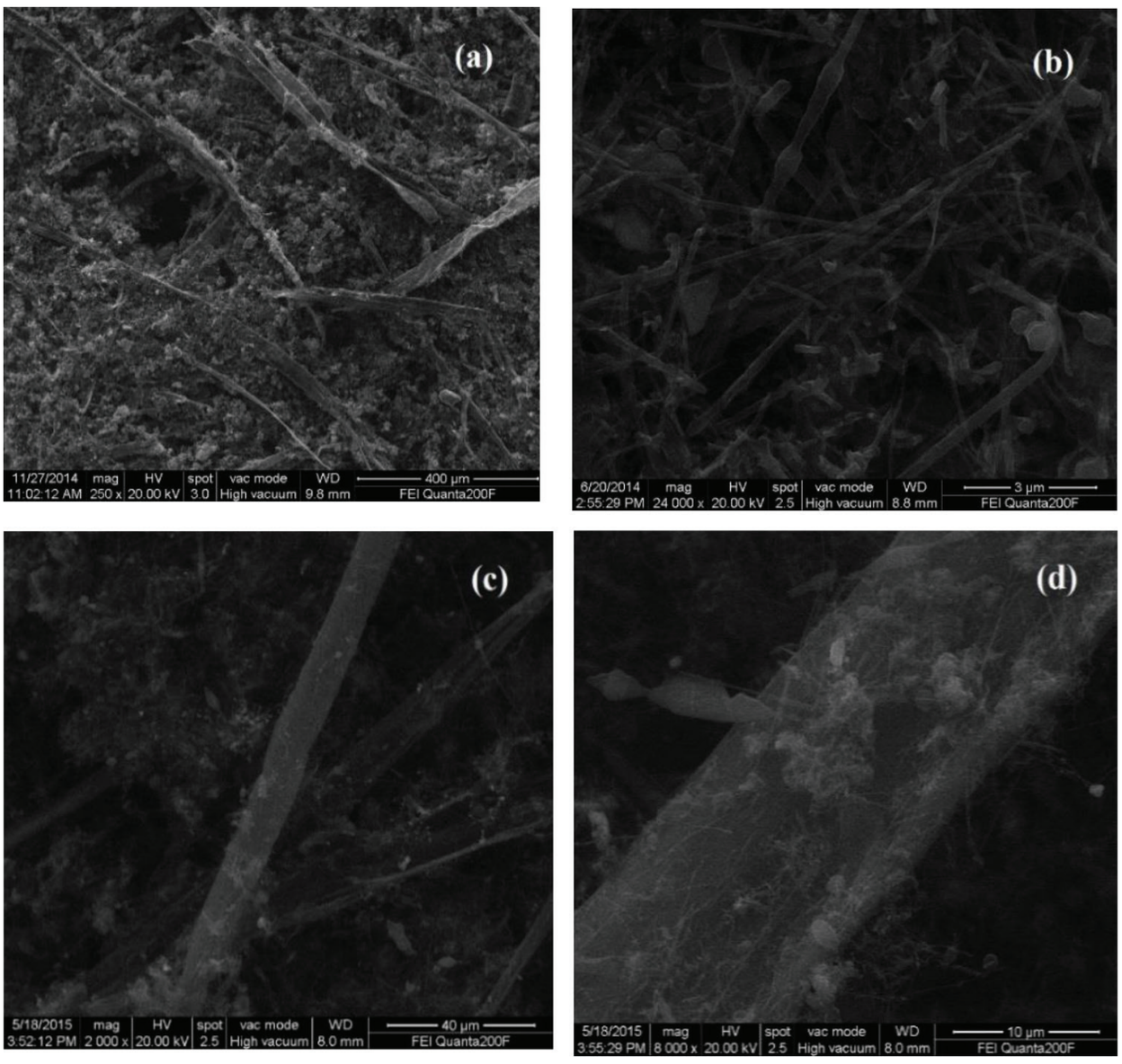

Figure 32. SEM images of (a,b) CNT/CP and (c,d) CNT/CCP electrodes.

http://dx.doi.org/10.5772/intechopen.71916

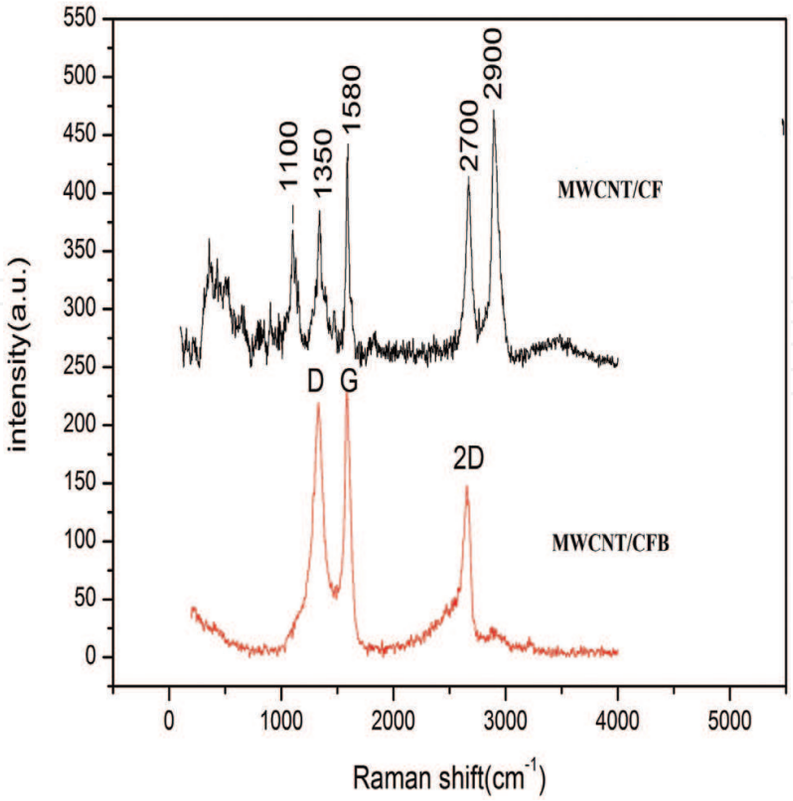

Figure 33. Raman spectra of CNT/CP and CNT/CCP electrodes.

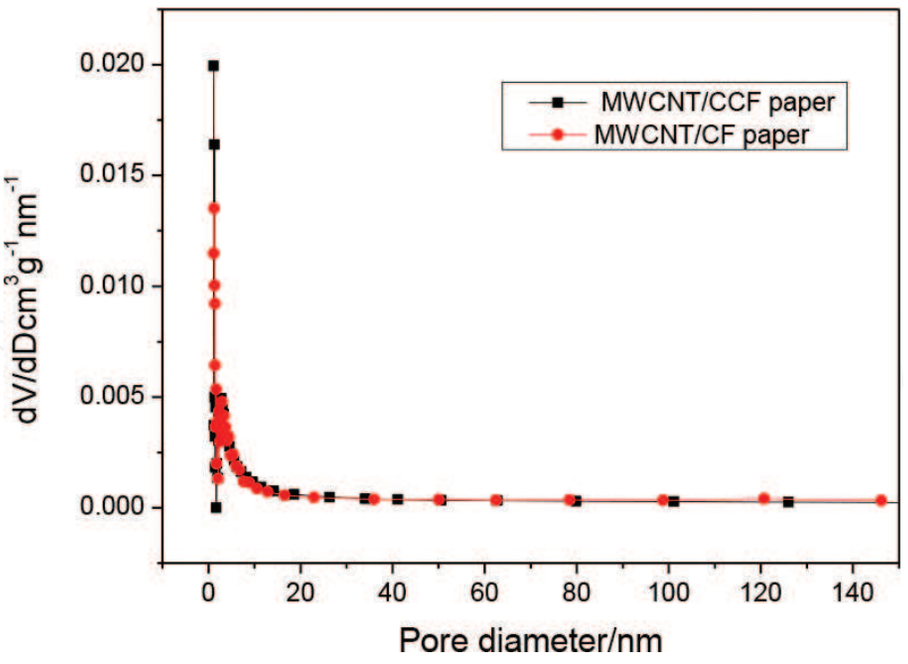

Figure 34. Pore diameter distribution for the CNT/CP and the CNT/CCP.

The electrochemical performance of the electrodes has been investigated by cyclic voltammetry (CV) (**Figure 35a,b**) with the voltage range of 0–2.5 V at four different scan rates of 5, 30, 50, and 100 mV/s. The CV curve of electric double layer capacitor is rectangular [131, 132].

However, the CV curve of CNT/CP (**Figure 35a**) electrodes presented a reduction peak without oxidation peak. The reduction reaction was related to the iron-based catalyst metals and reaction of lithium ions in electrolyte. Moreover, the irreversible redox reaction of iron and irreversible capacity of CNTs contributed to the absence of oxidation peak [121, 133–135]. The CV curve of CNT/CCP (**Figure 35b**) electrodes presented a perfect redox peak, which was related to faraday reaction. The no-carbon elements of CNT/CCP electrodes were evaporated in the process of carbonization. This is beneficial to the intercalate and de-intercalate of lithium ions in amorphous carbon particles [64, 131–136].

Specific capacitance and scan rate curves of CNT/CP and CNT/CCP are shown in **Figure 36**. The specific capacitance (Cscv) of the symmetric supercapacitor was calculated according to the following equation: Cscv = 2S/[(U2-U1) mν]. Cscv is the specific capacitance of the capacitor in F/g, S is the total voltammetric sweeps area during CV, (U2–U1) is the range of voltage, m is the active material mass per electrode, and ν is the scan rate.

With the increase of scan rate, the capacity of supercapacitor was decreased. The capacitance of MWCNT/CF electrode was 24 and 4.55 F/g at a scan rate 5 and 100 mV/s, respectively. By contrast, the capacitance of CNT/CCF electrode corresponds to 43 and 26 F/g at a scan rate 5 and 100 mV/s, respectively. The results show that carbonized electrode (CNT/CCF) exhibited a better capacitance performance than uncarbonized electrodes (CNT/CF).

Figure 37 shows the electrochemical impedance spectroscope (EIS) of the supercapacitors, and the EIS was measured at the same open circuit potential of 2.5 V. The interception of the real axis represents the solution resistance. The solution resistance of the supercapacitor is 16 Ω. The semicircle in the high frequency region presented the charge transfer resistance of electrode. The charge transfer resistance of carbonized electrode (CNT/CCF) is only 3 Ω, which suggested an excellent transfer resistance performance. The impedance curves showed a straight line slopes at low frequency region, which also suggested a good capacitive performance of carbonized electrodes. Absence of semicircle at low frequency means low contact resistance between collector and electrode plates [9]. The electrical conductivity of CNT/CCF electrode was tested by four-point probe resistance meter. The electrical conductivity was obviously raised from 714.3 to 325.1 S/m after carbonization.

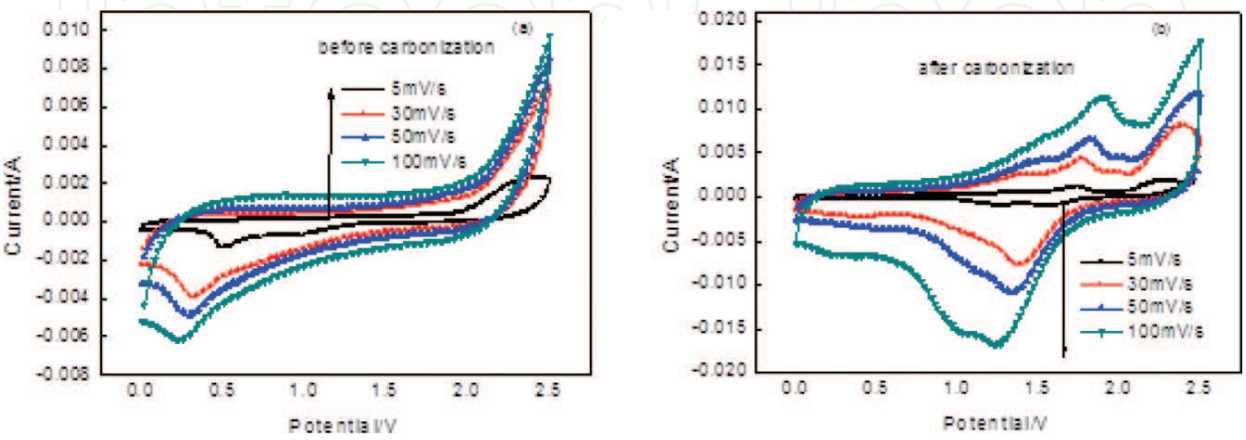

Figure 35. Cyclic voltammetry curves of (a) CNT/CP and (b) CNT/CCP electrodes.

http://dx.doi.org/10.5772/intechopen.71916

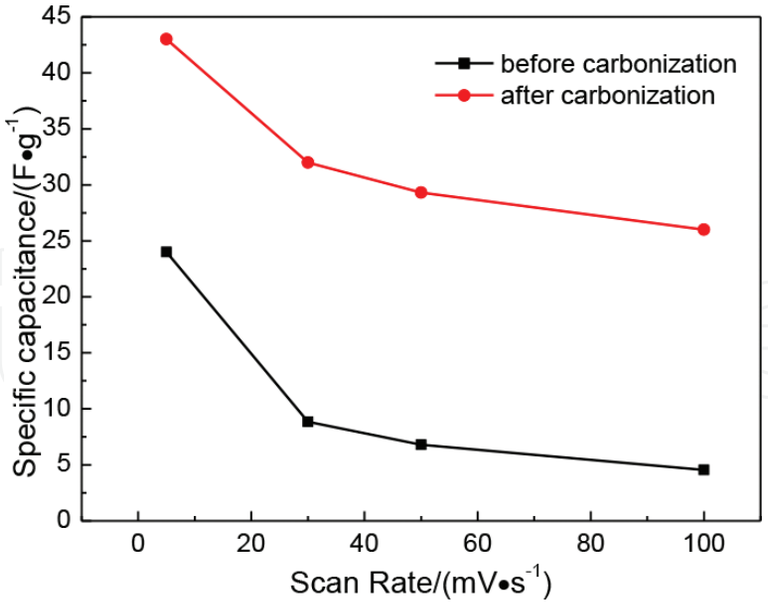

Figure 36. The specific capacitance of the supercapacitors vs. scan rate for CNT/Cp electrode and CNT/CCp electrode.

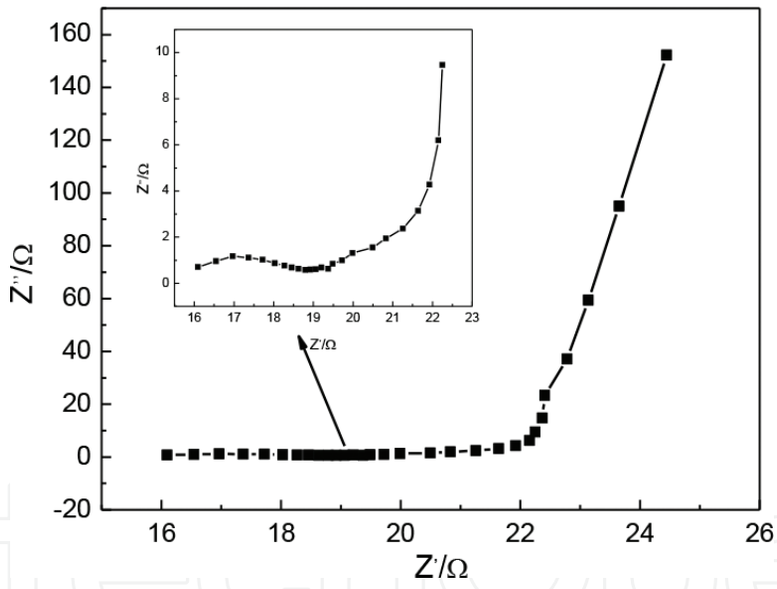

Figure 37. Electrochemical impedance spectroscope (EIS) of supercapacitor with carbonized electrode.

The specific capacitance (Cscv) of the two capacitors was calculated based on the charge/discharge profiles according to the following equation: Cscd = [2I]/[m(dV/dt)], where Cscd is the specific capacitance of the capacitors in F/g, I is the current in A, m is the mass of the active material in the capacitors in gram, and dV/dt is the slope of the discharge curve after the IR drop.

The charge/discharge curves of the CNT/CF and CNT/CCF electrodes were compared using different current density of 50, 100, 200, and 400 mA/g (**Figure 38**). The Cscd decreased as the current density increased. For CNT/CF electrode (**Figure 38a**), the capacity decreased from 17

F/g (50 mA/g), 12.8 F/g (100 mA/g), and 13 F/g (200 mA) to 12 F/g (400 mA/g). For CNT/CCF electrode (**Figure 38b**), the capacity decreased from 39 F/g (50 mA/g), 38 F/g (100 mA/g), 38 F/g (200 mA/g), 32.9 F/g (400 mA/g) to 29.2F/g (800 mA/g). The testing results indicated that the performance of supercapacitor was greatly improved after carbonization of electrodes. The curves of charge/discharge are not straight lines due to Faraday reaction.

Continuous charge-discharge was carried out for the CNT/CCP supercapacitor at constant current of 400 mA/g for 500 cycles (**Figure 39**). **Figure 39** shows the change in specific capacitance in 500 cycles. The CNT/CCP supercapacitor showed a progressive decrease in cycles. The specific capacitance still holds 74.6% after 500 cycles, which may be contributed to good wetting of electrolyte to electrodes and big interface areas between electrodes and electrolyte.

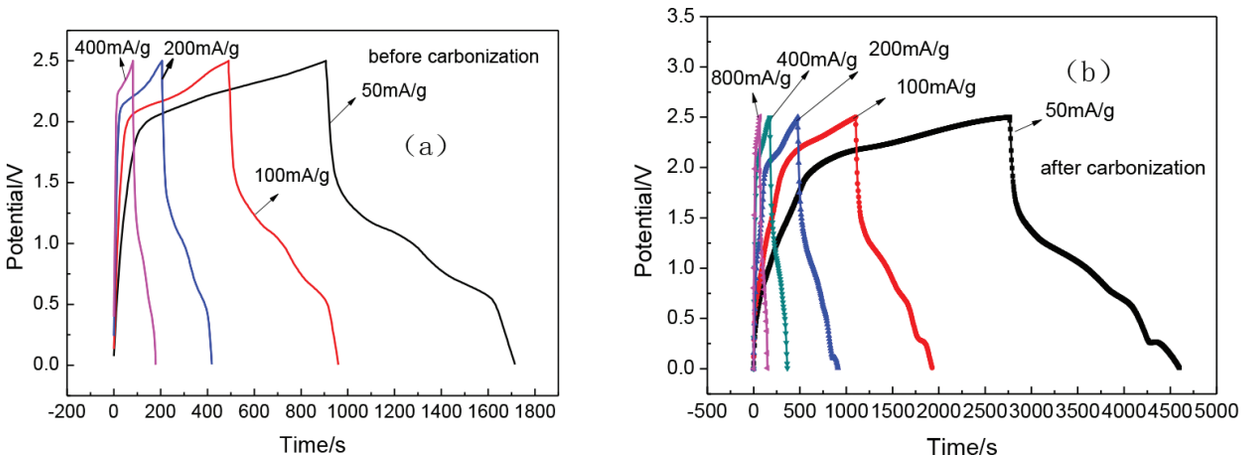

Figure 38. Galvanostatic charge/discharge curves of (a) CNT/CF and (b) CNT/CCP electrodes.

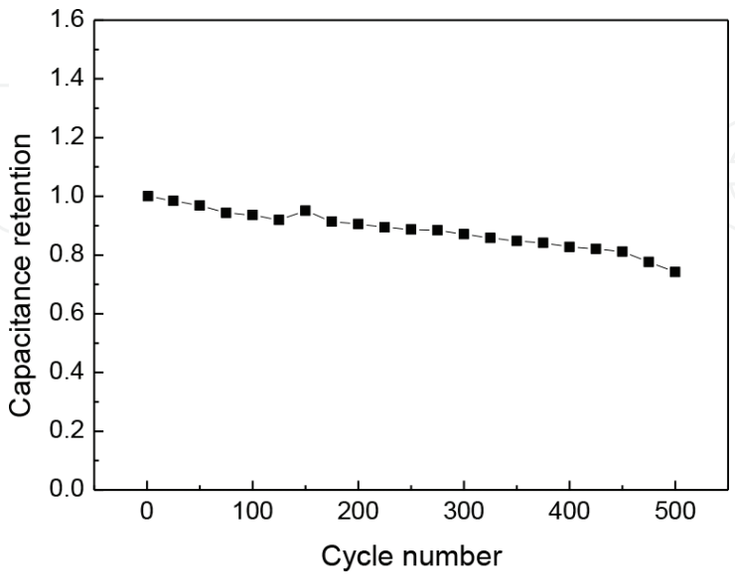

Figure 39. Capacitance retention of the carbonized CNT/CCP electrodes.

3.5.3. Conclusions

MWCNT/cellulose fiber electrodes provide 3D porous network structure and large interfacial area between electrode and electrolyte. Capacitance performance could be improved by the electrode and electrolyte's intimate contact. After carbonization treatment, the CNT/CCP electrodes have a higher performance of capacitance. The improvement is contributed to a better absorption of electrolyte, lower resistance of carbonized electrodes, and increase of effective interface area for forming of double layers. When the current density is 50 mA/g, the maximum specific capacitance of a unit capacitor reached 39 F/g by galvanization charge/discharge measurement, while the minimum specific capacitance of unit capacitor reached 24 F/g at a scan rate 5 mV/s of cyclic voltammetry measurement. The capacitance holds 74.6% after 500 cycles at a current density of 400 mA/g.

4. Outlook for CNTs and CNTCP in primary/second batteries and capacitors

In summary, our researches were reported of CNTs and CNTCP for primary/second batteries and supercapacitors applications. It has a great potential application value for the porous carbon nanotube-cellulose papers as current collectors and electrodes in lithium ion battery and supercapacitors. However, there are still some problems to be solved. The pore size and porosity and carbonization process of CNTCPs needed to be innovated to improve the strength and electrical conductivity. New high flexibility and strength of nanofibers need to be developed to adapt to electrolytes, as the cellulose papers are easily destroyed in liquid. The further investigations need to be done to overcome technological barriers for industrial applications of CNTCP in LIBs and SCs.

Author details

Xiaogang Sun*, Manyuan Cai, Long Chen, Zhiwen Qiu, Jie Wang, Xu Li and Wei Chen

*Address all correspondence to: xiaogangsun@163.com

School of Mechatronics Engineering, Nanchang University, Nanchang, China

References

[1] Zhang Y, Zhao Y, Konarov A, et al. Effect of mesoporous carbon microtube prepared by carbonizing the poplar catkin on sulfur cathode performance in Li/S batteries. Journal of Alloys and Compounds. 2015;**619**:298-302

[2] Liang J, Sun ZH, Li F, et al. Carbon materials for Li–S batteries: Functional evolution and performance improvement. Energy Storage Materials. 2015;**2**:76-106

[3] Wang C, Chen JJ, Shi YN, et al. Preparation and performance of a core–shell carbon/sulfur material for lithium/sulfur battery. Electrochimica Acta. 2010;**55**(23):7010-7015

[4] Li Y, Zhan H, Liu S, et al. Electrochemical properties of the soluble reduction products in rechargeable Li/S battery. Journal of Power Sources. 2010;**195**(9):2945-2949

[5] Jin S, Xin S, Wang L, et al. Covalently connected carbon nanostructures for current hosts in both the cathode and anode of Li-S batteries. Advanced Materials. 2016:**28**(41)

[6] Zhang J, Yang N, Yang X, et al. Hollow sulfur@graphene oxide core–shell composite for high-performance Li–S batteries. Journal of Alloys and Compounds. 2015;**650**:604-609

[7] Stoeck U, Balach J, Klose M, et al. Reconfiguration of lithium sulphur batteries: "Enhancement of Li–S cell performance by employing a highly porous conductive separator coating". Journal of Power Sources. 2016;**309**:76

[8] Wu Y, Gao M, Li X, et al. Preparation of mesohollow and microporous carbon nanofiber and its application in cathode material for lithium–sulfur batteries. Journal of Alloys and Compounds. 2014;**608**(10):220-228

[9] Choi S, Kim J, Eom M, et al. Application of a carbon nanotube (CNT) sheet as a current host for all-solid-state lithium batteries. Journal of Power Sources. 2015;**299**:70-75

[10] Hu L, Liu N, Eskilsson M, et al. Silicon-conductive nanohost for Li-ion batteries. Nano Energy. 2013;**2**(1):138-145

[11] Fang J, Qin F, Li J, et al. Improved performance of sulfur cathode by an easy and scale-up coating strategy. Journal of Power Sources. 2015;**297**:265-270

[12] Lee SK, Oh SM, Park E, et al. Highly cyclable lithium-Sulfur batteries with a dual-type Sulfur cathode and a lithiated Si/SiOx nanosphere anode. Nano Letters. 2015;**15**(5)

[13] Zhe Y, Peng HJ, Huang JQ, et al. Hierarchical free-standing carbon-nanotube host electrodes with ultrahigh Sulfur-loading for lithium–sulfur batteries. Advanced Functional Materials. 2014;**24**(39):6105-6112

[14] Wei W, Wang J, Zhou L, et al. CNT enhanced sulfur composite cathode material for high rate lithium battery. Electrochemistry Communications. 2011;**13**(5):399-402

[15] Chen JJ, Jia X, She QJ, et al. The preparation of nano-sulfur/MWCNTs and its electrochemical performance. Electrochimica Acta. 2010;**55**(27):8062-8066

[16] Waag W, Käbitz S, Sauer DU. Experimental investigation of the lithium-ion battery impedance characteristic at various conditions and aging states and its influence on the application. Applied Energy. 2013;**102**(2):885-897

[17] Lou X, Wang Y, Yuan C, et al. Template-free synthesis of SnO_2 hollow nanostructures with high lithium storage capacity. Advanced Materials. 2006;**18**(17):2325-2329

[18] Wang Y, Zeng H, Lee J. Highly reversible lithium storage in porous SnO_2, nanotubes with coaxially grown carbon nanotube Overlayers. Advanced Materials. 2006;**18**(5):645-649

[19] Li L, Yin X, Liu S, et al. Electrospun porous SnO_2, nanotubes as high capacity anode materials for lithium ion batteries. Electrochemistry Communications. 2010;**12**(10): 1383-1386

[20] Chen JS, Yan LC, Chen YT, et al. SnO_2 nanoparticles with controlled carbon Nanocoating as high-capacity anode materials for lithium-ion batteries. Journal of Physical Chemistry C. 2009;**113**(47):20504-20508

[21] Wang MS, Lei M, Wang ZQ, et al. Scalable preparation of porous micron-SnO_2/C composites as high performance anode material for lithium ion battery. Journal of Power Sources. 2016;**309**:238-244

[22] Xia G, Li N, Li D, et al. Graphene/Fe_2O_3/SnO_2 ternary nanocomposites as a high-performance anode for lithium ion batteries. ACS Applied Materials & Interfaces. 2013;**5**(17): 8607-8614

[23] Srinivasan NR, Mitra S, Bandyopadhyaya R. Improved electrochemical performance of SnO_2-mesoporous carbon hybrid as a negative electrode for lithium ion battery applications. Physical Chemistry Chemical Physics PCCP. 2014;**16**(14):6630-6640

[24] Yang L, Chen K, Dong T, et al. One-pot synthesis of SnO_2/C Nanocapsules composites as anode materials for lithium-ion batteries. Journal of Nanoscience and Nanotechnology. 2016;**16**(2):1768-1774

[25] Han F, Li WC, Li MR, et al. Fabrication of superior-performance SnO_2@C composites for lithium-ion anodes using tubular mesoporous carbon with thin carbon walls and high pore volume. Journal of Materials Chemistry. 2012;**22**(19):9645-9651

[26] Yao J, Shen X, Wang B, et al. In situ, chemical synthesis of SnO_2 –graphene nanocomposite as anode materials for lithium-ion batteries. Electrochemistry Communications. 2009;**11**(10):1849-1852

[27] Zhou X, Wan LJ, Guo Y. Binding SnO_2, Nanocrystals in nitrogen-doped Graphene sheets as anode materials for lithium-ion batteries. Advanced Materials. 2013;**25**(15):2152-2157

[28] Song H, Li X, Cui Y, et al. Controllable lithium storage performance of tin oxide anodes with various particle sizes. International Journal of Hydrogen Energy. 2015;**40**(41): 14314-14321

[29] Han S, Jang B, Kim T, et al. Simple synthesis of hollow tin dioxide microspheres and their application to lithium-ion battery anodes. Advanced Functional Materials. 2005;**15**(11): 1845-1850

[30] Park M-S, Wang G-X, Kang Y-M, et al. Preparation and electrochemical properties of SnO_2 nanowires for application in lithium-ion batteries. Angewandte Chemie. 2007; **119**(5):764-767

[31] Yang Z, Du G, Feng C, et al. Synthesis of uniform polycrystalline tin dioxide nanofibers and electrochemical application in lithium-ion batteries. Electrochimica Acta. 2010;**55**(19):5485-5491

[32] Park M-S, Kang Y-M, Wang G-X, et al. The effect of morphological modification on the electrochemical properties of SnO_2 Nanomaterials. Advanced Functional Materials. 2008;**18**(3):455-461

[33] Wang C, Zhou Y, Ge M, et al. Large-scale synthesis of SnO_2 Nanosheets with high lithium storage capacity. Journal of the American Chemical Society. 2009;**132**(1):46-47

[34] Yu Y, Chen CH, Shi Y. A tin-based amorphous oxide composite with a porous, spherical, multideck-cage morphology as a highly reversible anode material for lithium-ion batteries. Advanced Materials. 2007;**19**(7):993-997

[35] Wu GT, Wang CS, Zhang XB, et al. Lithium insertion into cu O/carbon nanotubes. Journal of Power Sources. 1998;**75**(1):175-179

[36] Cui G, Hu Y-S, Zhi L, et al. A one-step approach towards carbon-encapsulated hollow tin nanoparticles and their application in lithium batteries. Small. 2007;**3**(12):2066-2069

[37] Derrien G, Hassoun J, Panero S, et al. Nanostructured Sn–C composite as an advanced anode material in high-performance lithium-ion batteries. Advanced Materials. 2007; **19**(17):2336-2340

[38] Jung YS, Lee KT, Ryu JH, et al. Sn-carbon Core-Shell powder for anode in lithium secondary batteries. Journal of the Electrochemical Society. 2005;**152**(7):A1452-A1457

[39] Marcinek M, Hardwick LJ, Richardson TJ, et al. Microwave plasma chemical vapor deposition of nano-structured Sn/C composite thin-film anodes for Li-ion batteries. Journal of Power Sources. 2007;**173**(2):965-971

[40] Lee KT, Jung YS, Oh SM. Synthesis of tin-encapsulated spherical hollow carbon for anode material in lithium secondary batteries. Journal of the American Chemical Society. 2003;**125**(19):5652-5653

[41] Hassan FM, Chen Z, Yu A, et al. Sn/SnO_2, embedded in mesoporous carbon nanocomposites as negative electrode for lithium ion batteries. Electrochimica Acta. 2013;**87**(1): 844-852

[42] Iijima S. Helical microtubules of graphitic carbon. Nature. 1991;**354**(6348):56-58

[43] Landi BJ, Dileo RA, Schauerman CM, et al. Multi-walled carbon nanotube paper anodes for lithium ion batteries. Journal of Nanoscience and Nanotechnology. 2009;**9**(6):3406-3410

[44] Wang CS, Wu GT, Li WZ. Lithium insertion in ball-milled graphite. Journal of Power Sources. 1998;**76**(1):1-10

[45] de las Casas C, Li W. A review of application of carbon nanotubes for lithium ion battery anode material. Journal of Power Sources. 2012;**208**:74-85

[46] Holzapfel M, Buqa H, Hardwick LJ, et al. Nano silicon for lithium-ion batteries. Electrochimica Acta. 2006;**52**(3):973-978

[47] Liang B, Liu Y, Xu Y. Silicon-based materials as high capacity anodes for next generation lithium ion batteries. Journal of Power Sources. 2014;**267**:469-490

[48] Huggings RA, Cui YI. High-performance lithium battery anodes using silicon nanowires. Materials for sustainable energy: A collection of peer-reviewed research and review articles from nature publishing group. 2011;**187**

[49] Zhang Y, Zhang XG, Zhang HL, et al. Composite anode material of silicon/graphite/carbon nanotubes for Li-ion batteries. Electrochimica Acta. 2006;**51**(23):4994-5000

[50] Khomenko VG, Barsukov VZ. Characterization of silicon-and carbon-based composite anodes for lithium-ion batteries. Electrochimica Acta. 2007;**52**(8):2829-2840

[51] Kim T, Mo YH, Nahm KS, et al. Carbon nanotubes (CNTs) as a buffer layer in silicon/CNTs composite electrodes for lithium secondary batteries. Journal of Power Sources. 2006;**162**(2):1275-1281

[52] Zhou Z, Xu Y, Liu W, et al. High capacity Si/DC/MWCNTs nanocomposite anode materials for lithium ion batteries. Journal of Alloys and Compounds. 2010;**493**(1):636-639

[53] Luo Z, Fan D, Liu X, et al. High performance silicon carbon composite anode materials for lithium ion batteries. Journal of Power Sources. 2009;**189**(1):16-21

[54] Zuo P, Yin G, Yang Z, et al. Improvement of cycle performance for silicon/carbon composite used as anode for lithium ion batteries. Materials Chemistry and Physics. 2009; **115**(2):757-760

[55] Khomenko VG, Barsukov VZ, Doninger JE, et al. Lithium-ion batteries based on carbon–silicon–graphite composite anodes. Journal of Power Sources. 2007;**165**(2):598-608

[56] Dimov N, Xia Y, Yoshio M. Practical silicon-based composite anodes for lithium-ion batteries: Fundamental and technological features. Journal of Power Sources. 2007;**171**(2):886-893

[57] Lam P, Yazami R. Physical characteristics and rate performance of (CF x) n (0.33< x< 0.66) in lithium batteries. Journal of Power Sources. 2006;**153**(2):354-359

[58] Dose WM, Donne SW. Optimising heat treatment environment and atmosphere of electrolytic manganese dioxide for primary Li/MnO_2 batteries. Journal of Power Sources. 2014;**247**:852

[59] Nakajima T. Fluorine compounds as energy conversion materials. Journal of Fluorine Chemistry. 2013;**149**:104-111

[60] Eweka EI, Giwa CO, Mepsted GO, Green K, Scattergood D. Development of high energy density small flat spiral cells and battery pack based on lithium/ carbon monofluoride (Li/CFx). Journal of Power Sources. 2006;**162**:841

[61] Zhang Q, D'Astorg S, Xiao P, Zhang X, Lu L. Carbon-coated FG for high energy and high power densities primary lithium batteries. Journal of Power Sources. 2010;**195**:2914

[62] Zhang SS, Foster D, Read J. Enhancement of discharge performance of Li/CFx cell by thermal treatment of CFx cathode material. Journal of Power Sources. 2009;**188**:601

[63] Dubois M, Guérin K, Zhang W, et al. Tuning the discharge potential of fluorinated carbon used as electrode in primary lithium battery. Electrochimica Acta. 2012;**59**(4):485-491

[64] Pasta M, Mantia FL, Hu L, et al. Aqueous Supercapacitors on conductive cotton. Nano Research. 2010;**3**(6):452-458

[65] Kang YJ, Chung H, Kim W. 1.8-V flexible supercapacitors with asymmetric configuration based on manganese oxide, carbon nanotubes, and a gel electrolyte. Synthetic Metals. 2013;**166**(4):40-44

[66] Zhu Z, Hu Y, Hao J, et al. A three-dimensional ordered mesoporous carbon/carbon nanotubes nanocomposites for supercapacitors. Journal of Power Sources. 2014;**246**(3):402-408

[67] Chuang, Peng, Shengwen, et al. Carbon nanotube and conducting polymer composites for supercapacitors. Progress in Natural Science. 2008;**18**(7):777-788

[68] Chao, Zheng, Weizhong, et al. Carbon nanotubes for supercapacitors: Consideration of cost and chemical vapor deposition techniques. Journal of Natural Gas Chemistry. 2012;**21**(3):233-240

[69] Yin Y, Liu C, Fan S. A new type of secondary hybrid battery showing excellent performances. Nano Energy. 2015;**12**:486-493

[70] Ruch PW, Kötz R, Wokaun A. Electrochemical characterization of single-walled carbon nanotubes for electrochemical double layer capacitors using non-aqueous electrolyte. Electrochimica Acta. 2009;**54**(19):4451-4458

[71] Wang G, Ling Y, Qian F, et al. Enhanced capacitance in partially exfoliated multi-walled carbon nanotubes. Journal of Power Sources. 2011;**196**(11):5209-5214

[72] Yun TG, Oh M, Hu L, et al. Enhancement of electrochemical performance of textile based supercapacitor using mechanical pre-straining. Journal of Power Sources. 2013;**244**(4): 783-791

[73] Kötz R, Carlen M. Principles and applications of electrochemical capacitors. Electrochimica Acta. 2000;**45**(15-16):2483-2498

[74] Wang H, Cheng P, Feng P, et al. Facile synthesis of MnO 2 /CNT nanocomposite and its electrochemical performance for supercapacitors. Materials Science and Engineering B. 2011;**176**(14):1073-1078

[75] Smithyman J, Liang R. Flexible supercapacitor yarns with coaxial carbon nanotube network electrodes. Materials Science and Engineering B. 2014;**184**(5):34-43

[76] Ge D, Yang L, Fan L, et al. Foldable supercapacitors from triple networks of macroporous cellulose fibers, single-walled carbon nanotubes and polyaniline nanoribbons. Nano Energy. 2015;**11**:568-578

[77] Youn HC, Park SH, Roh KC, et al. Highly dispersible surface-unzipped multi-walled carbon nanotubes as binder-free electrodes for supercapacitor applications. Current Applied Physics. 2015;**15**:S21-S26

[78] Wang G, Liang R, Liu L, et al. Improving the specific capacitance of carbon nanotubes-based supercapacitors by combining introducing functional groups on carbon nanotubes with using redox-active electrolyte. Electrochimica Acta. 2014;**115**(3):183-188

[79] Portet C, Taberna PL, Simon P, et al. Influence of carbon nanotubes addition on carbon–carbon supercapacitor performances in organic electrolyte. Journal of Power Sources. 2005;**139**(1-2):371-378

[80] Zheng C, Qian W, Wei F. Integrating carbon nanotube into activated carbon matrix for improving the performance of supercapacitor. Materials Science and Engineering B. 2012;**177**(13):1138-1143

[81] Fang R, Zhao S, Hou P, et al. 3D interconnected electrode materials with ultrahigh areal Sulfur loading for Li-S batteries. Advanced Materials. 2016;**28**(17):3374-3382

[82] Chen SR, Zhai YP, Xu GL, et al. Ordered mesoporous carbon/sulfur nanocomposite of high performances as cathode for lithium–sulfur battery. Electrochimica Acta. 2011;**56**(26):9549-9555

[83] Zhu Y, Xu G, Zhang X, et al. Hierarchical porous carbon derived from soybean hulls as a cathode matrix for lithium-sulfur batteries. Journal of Alloys and Compounds; 2016

[84] Ghazi ZA, Zhu L, Wang H, et al. Efficient polysulfide chemisorption in covalent organic frameworks for high-performance lithium-Sulfur batteries. Advanced Energy Materials. 2016

[85] Fang R, Zhao S, Pei S, et al. Toward More Reliable Lithium–Sulfur Batteries: An all-Graphene cathode structure. Acs Nano. 2016;**10**(9):8676-8682

[86] Liu X, Zhang Q, Zhang S, et al. Hierarchical nanostructured composite cathode with carbon nanotubes as conductive scaffold for lithium-sulfur batteries. Journal of Energy Chemistry. 2013;**22**(2):341-346

[87] Zheng W, Liu YW, Hu XG, et al. Novel nanosized adsorbing sulfur composite cathode materials for the advanced secondary lithium batteries. Electrochimica Acta. 2006;**51**(7):1330-1335

[88] Nazar LF, Cuisinier M, Pang Q. Lithium-sulfur batteries. MRS Bulletin. 2014;**39**(5 (Lithium Batteries and Beyond)):436-442

[89] Tessonnier JP, Rosenthal D, Hansen TW, et al. Analysis of the structure and chemical properties of some commercial carbon nanostructures. Carbon. 2009;**47**(7):1779-1798

[90] Zhu X, Zhu Y, Murali S, et al. Reduced graphene oxide/tin oxide composite as an enhanced anode material for lithium ion batteries prepared by homogenous coprecipitation. Journal of Power Sources. 2011;**196**(15):6473-6477

[91] Miao C, Liu M, He YB, et al. Monodispersed SnO_2 nanospheres embedded in framework of graphene and porous carbon as anode for lithium ion batteries. Energy Storage Materials. 2016;**3**:98-105

[92] Wen Z, Zheng F, Liu K. Synthesis of porous SnO_2, nanospheres and their application for lithium-ion battery. Materials Letters. 2012;**68**(2):469-471

[93] Hu R, Sun W, Zhu M. Microstructure and Composition Tuning: Enhancing Reversibility of SnO_2 based anodes and reducing their initial capacity loss. The Electrochemical Society. 2014;(2):386-386

[94] Wang Y, Su D, Wang C, et al. SnO_2 @MWCNT nanocomposite as a high capacity anode material for sodium-ion batteries. Electrochemistry Communications. 2013;**29**(10):8-11

[95] Meng FL, Li HH, Kong LT, et al. Parts per billion-level detection of benzene using SnO_2/graphene nanocomposite composed of sub-6 nm SnO_2, nanoparticles. Analytica Chimica Acta. 2012;**736**(14):100

[96] Deshpande R, Cheng YT, Verbrugge MW. Modeling diffusion-induced stress in nanowire electrode structures. Journal of Power Sources. 2010;**195**(15):5081-5088

[97] Pushparaj VL, Shaijumon MM, Kumar A, et al. Flexible energy storage devices based on nanocomposite paper. Proceedings of the National Academy of Sciences. 2007; **104**(34):13574-13577

[98] Gohier A, Laïk B, Kim KH, et al. High-rate capability silicon decorated vertically aligned carbon nanotubes for Li-ion batteries. Advanced Materials. 2012;**24**(19):2592-2597

[99] Lee JH, Kim WJ, Kim JY, et al. Spherical silicon/graphite/carbon composites as anode material for lithium-ion batteries. Journal of Power Sources. 2008;**176**(1):353-358

[100] Chen S, Shen L, Peter A, et al. Dual-functionalized double carbon shells coated silicon nanoparticles for high performance lithium-ion batteries. Advanced Materials. 2017:1605650

[101] Yang X, Wen Z, Zhang L, et al. Synthesis and electrochemical properties of novel silicon-based composite anode for lithium-ion batteries. Journal of Alloys and Compounds. 2008;**464**(1):265-269

[102] Yoon S, Lee S, Kim S, et al. Carbon nanotube film anodes for flexible lithium ion batteries. Journal of Power Sources. 2015;**279**:495-501

[103] Song B, Fang H, Yang J, et al. Intercalation and diffusion of lithium ions in a carbon nanotube bundle by ab initio molecular dynamics simulations. Energy & Environmental Science. 2011;**4**(4):1379-1384

[104] Gao H, Hou F, Zheng X, et al. Electrochemical property studies of carbon nanotube films fabricated by CVD method as anode materials for lithium-ion battery applications. Vacuum. 2015;**112**:1-4

[105] Ni JF, Zhou HH, Chen JT, et al. Study of current collectors for Li-ion batteries. Battery Bimonthly. 2005;**2**:128-130

[106] Gao L, Liu S, Dougal RA. Dynamic lithium-ion battery model for system simulation. IEEE Transactions on Components and Packaging Technologies. 2002;**25**(3):495-505

[107] Armand M, Tarascon JM. Building Better Batteries. Nature. 2008;**451**(7179):652-653

[108] Lee SW, Gallant BM, Lee Y, et al. Self-standing positive electrodes of oxidized few-walled carbon nanotubes for light-weight and high-power lithium batteries. Energy & Environmental Science. 2012;**5**(1):5437-5444

[109] Zheng D, Wu C, Li J, et al. Chemically shortened multi-walled carbon nanotubes used as anode materials for lithium-ion batteries. Physica E: Low-dimensional Systems and Nanostructures. 2013;**53**:155-160

[110] Scrosati B, Garche J. Lithium batteries: Status, prospects and future. Journal of Power Sources. 2010;**195**(9):2419-2430

[111] Marom R, Amalraj SF, Leifer N, et al. A review of advanced and practical lithium battery materials. Journal of Materials Chemistry. 2011;**21**(27):9938-9954

[112] Kwon YK, Tomanek D. Electronic and structural properties of multiwall carbon nanotubes. Physical Review B. 1998;**58**(24):16001-16004

[113] Ajayan PM. Nanotubes from carbon. Chemical Reviews. 1999;**99**(7):1787-1800

[114] Dai HJ. Carbon nanotubes: Opportunities and challenges. Surface Science. 2002;**500**(1-3): 218-222

[115] Baughman RH, Zakhidov AA, De Heer WA. Carbon nanotubes–the route toward applications. Science. 2002;**297**(5582):787-792

[116] Salajkove M, Valentini L, Zhou Q, et al. Tough nanopaper structures based on cellulose nanofibers and carbon nanotubes. Composites Science and Technology. 2013;**87**: 103-110

[117] Cheng Q, Song Z, Ma T, et al. Folding paper-based lithium-ion batteries for higher areal energy densities. Nano Letters. 2013;**13**(10):4969-4974

[118] Lee YS. Syntheses and properties of fluorinated carbon materials. Journal of Fluorine Chemistry. 2007;**128**(4):392-403

[119] Nobili L, Guglielmini A. Thermal stability and mechanical properties of fluorinated diamond-like carbon coatings. Surface and Coatings Technology. 2013;**219**:144-150

[120] Jayasinghe R, Thapa AK, Dharmasena RR, et al. Optimization of multi-walled carbon nanotube based CF x, electrodes for improved primary and secondary battery performances. Journal of Power Sources. 2014;**253**(5):404-411

[121] Ouyang Y, Cong LM, Chen L, et al. Raman study on single-walled carbon nanotubes and multi-walled carbon nanotubes with different laser excitation energies. Physica E: Low-dimensional Systems and Nanostructures. 2008;**40**(7):2386-2389

[122] Groult H, Nakajima T, Perrigaud L, et al. Surface-FG anode materials for Li-ion batteries. Journal of Fluorine Chemistry. 2005;**126**(7):1111-1116

[123] Mar M, Ahmad Y, Guérin K, et al. Fluorinated exfoliated graphite as cathode materials for enhanced performances in primary lithium battery. Electrochimica Acta. 2016

[124] Li Y. The improved discharge performance of Li/CFx batteries by using multi-walled carbon nanotubes as conductive additive. Journal of Power Sources. 2011;**196**(196): 2246-2250

[125] Nagasubramanian G, Sanchez B. A new chemical approach to improving discharge capacity of Li/(CF x) n, cells. Journal of Power Sources. 2007;**165**(2):630-634

[126] Pang C, Ding F, Sun W, et al. A novel dimethyl sulfoxide/1,3-dioxolane based electrolyte for lithium/carbon fluorides batteries with a high discharge voltage plateau. Electrochimica Acta. 2015;**174**:230-237

[127] Xu Y, Zhan L, Wang Y, et al. Fluorinated graphene as a cathode material for high performance primary lithium ion batteries. Carbon. 2015;**86**(1):79-85

[128] Wu C, Wang H, Liao C, et al. Enhanced performance of Li-O_2, battery based on CF x /C composites as cathode materials. Electrochimica Acta. 2015;**186**:631-641

[129] Guo W, Li X, Xu J, et al. Growth of highly nitrogen-doped amorphous carbon for Lithium-ion battery anode. Electrochimica Acta. 2015;**188**:414-420

[130] Delhaes P, Couzi M, Trinquecoste M, et al. A comparison between Raman spectroscopy and surface characterizations of multiwall carbon nanotubes. Carbon. 2006;**44**(14):3005-3013

[131] Yang C, Chen C, Pan Y, et al. Flexible highly specific capacitance aerogel electrodes based on cellulose nanofibers, carbon nanotubes and polyaniline. Electrochimica Acta. 2015;**182**:264-271

[132] Zhang J, Gao L. Dispersion of multiwall carbon nanotubes by sodium dodecyl sulfate for preparation of modified electrodes toward detecting hydrogen peroxide. Materials Letters. 2007;**61**(17):3571-3574

[133] Ng SH, Wang J, Guo ZP, et al. Single wall carbon nanotube paper as anode for lithium-ion battery. Electrochimica Acta. 2005;**51**(1):23-28

[134] Eom JY, Kwon HS, Liu J, et al. Lithium insertion into purified and etched multi-walled carbon nanotubes synthesized on supported catalysts by thermal CVD. Carbon. 2004; **42**(12):2589-2596

[135] Sivakkumar SR, Pandolfo AG. Carbon nanotubes/amorphous carbon composites as high-power negative electrodes in lithium ion capacitors. Journal of Applied Electrochemistry. 2014;**44**(1):105-113

[136] Morris RS, Dixon BG, Gennett T, et al. High-energy, rechargeable Li-ion battery based on carbon nanotube technology. Journal of Power Sources. 2004;**138**(1-2):277-280